COHESIVE ZONE MODELING OF FRACTURE OF SUSTAINABLE AND FUNCTIONALLY GRADED CONCRETE

BY

DANIEL WILLIAM SPRING

THESIS

Submitted in partial fulfillment of the requirements
for the degree of Master of Science in Civil Engineering
in the Graduate College of the
University of Illinois at Urbana-Champaign, 2011

Urbana, Illinois

Adviser:

Professor Glaucio H. Paulino

ABSTRACT

There is a constant demand from the industry to provide better, more situation dependent construction materials; materials which are able to satisfy strength requirements while also able to accommodate other design requirements such as ductility, fracture resistance, thermal resistance/insulation, etc. Functionally graded materials (FGMs) are one such material. This study investigates the fracture process of sustainable concrete, fiber reinforced concrete, and of functionally graded concrete slabs. Both two-dimensional and three-dimensional problems are analyzed.

The primary focus of the thesis is on sustainable, functionally graded concrete slabs, emphasizing the computational/mechanical aspects of fracture. A model of the slabs is developed; which incorporates a variety of cohesive zone models (CZMs) into an implicit, nonlinear finite element scheme. Intrinsic cohesive zone elements, with traction-separation relationships defined along the crack surface, are utilized to simulate mode I fracture of the slabs. Based on the load to crack mouth opening displacement (CMOD) relationships of the slab, one is able to optimize concrete properties and placement to reach predefined goals. A parametric study is conducted on the fracture parameters of the slab; the results of which show that the variations in the CZMs have a direct correlation with the overall behaviour of the slab.

Additionally, in conducting the experiments for the slabs, a new fracture test for concrete is developed. The attractive feature of the test is that it uses a specimen geometry which is easily obtained from in-situ concrete in the field. Technology exists which allows us to extract cylindrical cores from concrete structures at relative ease. This study proposes a specimen geometry which can easily be developed from these cylindrical cores called the disk-shaped compact tension (DCT) specimen. A series of experiments are conducted on the specimen, and computational simulations are carried out. A parametric study is done; the results of which, show that the specimen geometry is able to predict the mode I fracture properties of concrete, with both virgin and recycled aggregates, with relative accuracy and ease.

To Joan and Bill, and Joan and Bill

ACKNOWLEDGMENTS

I take this time to express my humble appreciation to my research and academic advisor, Professor Glaucio Paulino, for his continued advice, support and encouragement throughout the past two years. His hard work and constant courtesy to all his students has made him an inspiration to me and will continue to motivate me throughout my future.

I also owe a lot of my knowledge and contributions to Dr. Kyoungsoo Park. As a post-doctoral student who has charitably donated his time to act as a mentor, he has continuously assisted and guided me in my pursuit of understanding. I appreciate everything he has helped me with, from gaining a foundation on the basics to expanding my knowledge into areas previously unbeknownst to me.

I would like to express my gratitude to Professor Jeffery Roesler, and graduate student Armen N. Amirkhanian for their experimental work, and collaborations. Their dedication to accuracy in their work made it easier to have confidence in my own work.

I am also very thankful to my fellow group members and colleagues: Arun L. Gain, Cameron Talischi, Lauren Stromberg, Sofie Leon, Tam Nguyen, Tomas Zegard, Eshan Dave, and Junho Chun, for their continued support and aid in transitioning, not only academically but socially and culturally as well.

This thesis is supported in part by the National Science Foundation (NSF) through Grant CMMI #0800805. The information presented in this thesis is the sole opinion of the author and does not necessarily reflect the views of the sponsoring agency.

TABLE OF CONTENTS

LIST OF FIGURES

LIST OF TABLES

CHAPTER 1

INTRODUCTION

The overall focus of this thesis is to study the fracture of different types of concrete and of functionally graded concrete. To do this, the first step is to gain a working knowledge of the present state of fracture mechanics. One of the fracture mechanics models in use today, and the one used in this study, is the cohesive zone model. This Chapter introduces the concepts of: cohesive zone modeling, functionally graded materials, and what is known as “green” concrete. Finally, the structure of the thesis is briefly outlined.

1.1 Cohesive Zone Modeling

Concrete is composed of a mixture of aggregates and a binder or cement paste. In general, the cement paste and the aggregates are both brittle, but with different elastic moduli, and the bond between the two is relatively weak. Even though concrete is made up of brittle components, it displays a small degree of macroscopic ductility. This macroscopic ductility has been attributed to the development of finite sized zones of diffuse damage (Bažant 1991), otherwise known as fracture process zones, see Figure 1.1. Due to this observation, concrete is classified as a quasi-brittle material.

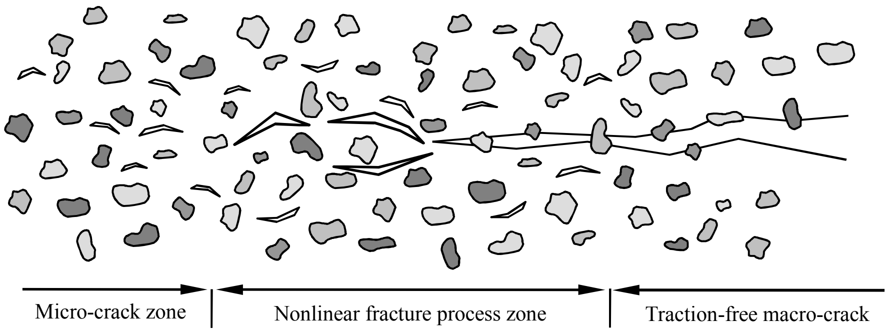

Figure 1.1: Progression of cracking in plain concrete.

The load-deformation relationship for quasi-brittle materials differs from linear elastic materials and perfectly plastic materials in that they exhibit a gradual decrease (or softening) in load carrying capacity after the peak load is achieved, see Figure 1.2. These nonlinearities in the load-deformation relationship are not able to be modeled accurately with the classic linear elastic fracture mechanics (LEFM) model. To overcome this, a model that accounts for the nonlinear fracture process zone is required. Several models have been developed, but the one used throughout this study is the cohesive zone model (CZM) (Barenblatt 1959, Dugdale 1960).

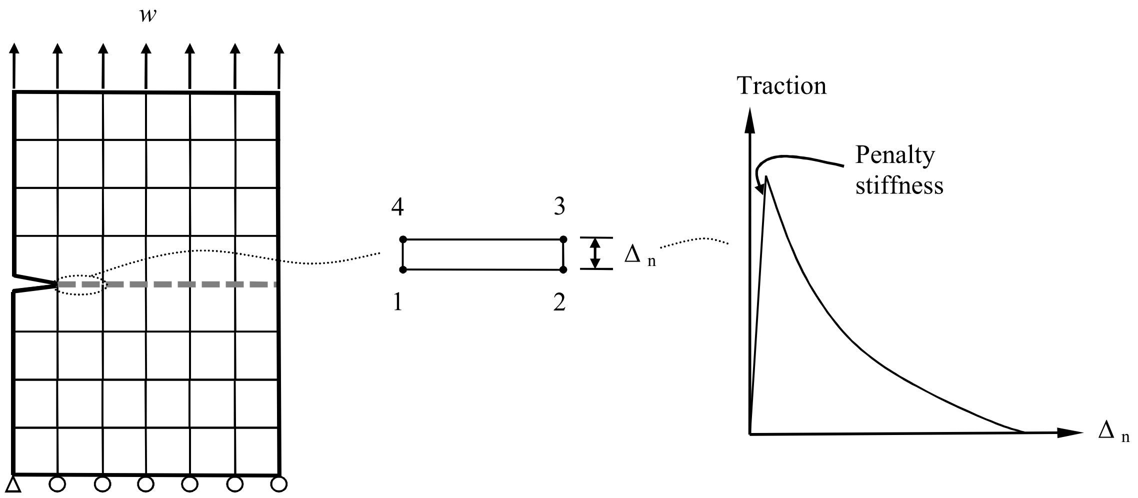

Figure 1.2: Use of two dimensional, mode I, cohesive elements in the finite element setting.

1.1.1 Finite Element Method of Modeling Cohesive Zone Elements

Cohesive zone models are, in the simplest sense, a relationship between crack opening displacement and surface tractions. In the finite element setting, they are inserted into a bulk model along the expected fracture path. They originally have a zero thickness (or zero opening width), and as the crack propagates through the model, they become active. A two dimensional, mode I example of a cohesive zone element is illustrated in Figure 1.2. The example is that of an intrinsic cohesive element. Intrinsic cohesive elements exist in the model prior to any crack separation occurring. This is accomplished through the use of an initial penalty stiffness, which causes a finite work to fracture (Xu and Needleman, 1994; Song et al., 2006a, 2006b; Park et al., 2008). Alternatively, extrinsic cohesive elements could have been used. Extrinsic cohesive elements are inserted after initial separation of the crack faces occurs, and do not include a penalty stiffness in their traction-separation relationship (Camacho and Ortiz, 1996; and Ortiz and Pandolfi, 1999). Both intrinsic and extrinsic elements are equally effective, but intrinsic elements are simpler to implement numerically, and are thus the chosen element type used in the present study.

1.2 Functionally Graded Materials

There are two distinct types of functionally graded materials. There are materials in which the properties continuously vary through the thickness of the material; otherwise known as functionally graded continuous materials (FGCMs). There are also materials in which there are distinct layers, with each layer containing different properties. This layered technique is the most common, as it is the most practical to implement physically (Ilschner 1996, 1999).

There are many current applications that use functionally graded materials. Some of the more popular application areas are in aerospace, power generation, microelectronics, and bioengineering. In the aerospace industry, functionally graded ceramic tiles are used as a thermal barrier material to protect space craft (Nemat-Alla, 2003). In the power generation industry, functionally graded materials (FGMs) are used to create more efficient photovoltaic cells (Berto A.M., 2007). In microelectronics, FGMs are used for optoelectronic devices; such as, photodetectors, and solar cells (Wosko et al., 2005). Similarly, in the bioengineering industry, functionally graded dental implants have been found to perform better than homogeneous implants (Watari et al., 1999).

1.2.1 Functionally Graded Concrete

Traditional homogeneous concrete mixtures are limited in their applications. Homogeneous mixtures consist of two basic components; cement paste and aggregates, each of which has a limited number of variables that can be modified to suit desired needs. The resulting concrete material has uniform bulk properties, which are often a trade-off of desired properties (Shen 2009). Alternatively, functionally graded concrete is composed of a continuously varying microstructure that can be engineered to meet specific requirements (Kim and Paulino, 2002), see Figure 1.3.

This thesis examines the application of functionally graded concrete slabs. Three different materials are used in the study: concrete with limestone aggregates, concrete with recycled aggregates, and fiber reinforced concrete. The present study emphasizes computational modeling, verification and, to a certain extent, validation.

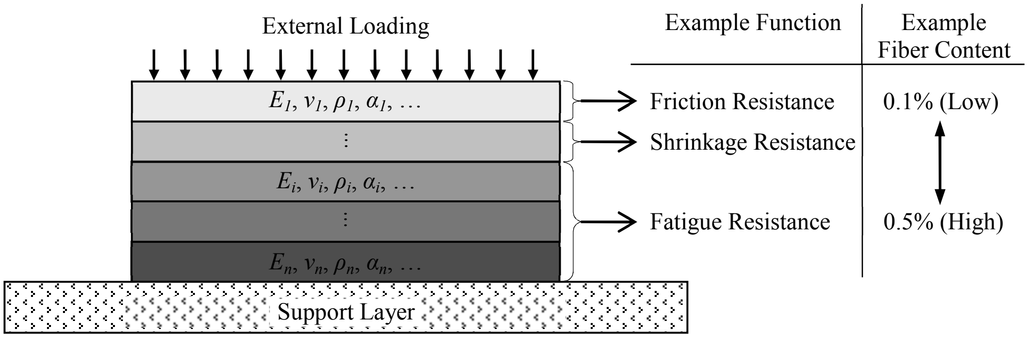

Figure 1.3: Schematic of a layered functionally graded material.

1.3 Green Concrete

Green concrete is a common term used to describe concrete that uses recycled concrete aggregate (RCA) in place of virgin limestone concrete aggregate (LCA). Recycled aggregates consist of waste concrete that is ground down into rubble (approximately 25mm in diameter) and used in place of limestone aggregates in the development of new concrete mixtures, see Figure 1.4. By diverting the waste concrete from landfills, we are able to extend the life of concrete structures (cradle to cradle).

(a) (b)

Figure 1.4: (a) Recycled concrete aggregates (b) Virgin limestone aggregates.

There has been a significant amount of research done to make the use of green concrete feasible. Most of the existing literature revolves around optimizing the mixture design to produce desirable physical and mechanical properties. Historically, recycled aggregates have been proposed for use in concrete as far back as the 1970’s (Nixon 1978). Some other important contributions to the knowledge of green concrete can be found in reports by T.C. Hansen (1986 and 1992), and in the ACI 555 Report (2002). Generally, the compressive strength, rupture strength, and elastic modulus are slightly lower than that of concrete containing standard limestone aggregates (RILEM Recommendation, 1994; ACI Committee 555 2002; Katz, 2003). Despite these shortcomings, there is a growing field of research in green concrete, as it presents a more environmentally friendly alternative than regular concrete, and is still suitable in many applications.

Some common characteristics of recycled aggregates include greater porosity and absorption, and lower density and strength than virgin limestone aggregates (Kou et al. 2007). A few studies have been done on the interfacial transition zone (ITZ), between the cement paste and the recycled aggregates; which find that the matrix to aggregate bond strength is generally weaker for recycled aggregates than it is for limestone aggregates (Otsuki et al., 2003; Poon et al., 2004; Kou et al., 2007). A study done by Poon et al. (2004) found that a higher compressive strength can be achieved when using recycled aggregates from high strength concrete than from normal strength concrete. In most cases, they observe that the strength of concrete with high strength recycled aggregates can meet the same strength as concrete with limestone aggregates. They attribute the difference to both the strength of the aggregates and the properties of the ITZ.

1.3.1 Fracture of Green Concrete

The different fracture parameters for RCA concrete, compared to LCA concrete, can be explained by changes in the ITZ and differences in the strength of the aggregates. As the bond strength between the aggregates and the cement paste increases, and the aggregates become weaker, the potential for cracks propagating through the aggregates increases. Giaccio and Zerbino (1998) showed that there is a large dependence between the fracture energy of LCA concrete and the cement-aggregate bond. Akçaolu et al. (2004) showed that there is a relationship between the aggregate properties and the strength of the ITZ and the corresponding compressive failure of concrete. Based on these studies, it can be expected that there is a difference in the failure of LCA and RCA concrete. This thesis tries to understand what the differences are, and how to predict them computationally.

1.4 Thesis Organization

The following thesis contains an additional 4 chapters. Chapter 2 focuses on the theory and code implementation of functionally graded materials, two-dimensional and three dimensional bilinear and tri-linear cohesive zone elements; and functionally graded cohesive zone elements. Chapter 3 introduces a new experimental test and corresponding cohesive zone, finite element model; which enables prediction of the fracture properties for various types of concrete. An emphasis is placed on the development of the model, and the comparison between fracture parameters for concrete with limestone aggregates and that with recycled aggregates. Chapter 4 studies the potential for the use of functionally graded slabs to satisfy multiple objectives; such as, ductility, fracture resistance, and strength. A series of layered slabs, with different properties in each layer, are simulated and the load-displacement and load-CMOD curves are analyzed to determine optimal combinations to satisfy specified requirements. Finally, Chapter 5 presents concluding comments and presents possible areas for future research.

CHAPTER 2

COMPUTATIONAL FRAMEWORK

It is imperative that one has an understanding of the background theory and required formulations to properly model and analyze the fracture of functionally graded concrete materials. The first step is to develop an understanding of the different methods of representing functionally graded finite elements. Then, to understand the affect cohesive elements have on the standard finite element formulation. The formulations for both two-dimensional and three-dimensional cohesive zone elements are included for completeness. Finally, functionally graded elements are combined with cohesive zone elements to produce functionally graded cohesive zone elements.

2.1 Isoparametric Graded Finite Elements

There exist numerous numerical methods to model FGMs. Ozturk and Erdogan (1997) proposed using integral equations; Pindera and Dunn (1997) proposed using higher-order models; Goldberg and Hopkins (1995) proposed using boundary elements, and Eischen (1987) proposed using finite elements. Each of these methods has been researched, modified, and adapted over the past several years, and has its own merits; but one of the simplest to implement, and the one used in this study, is the finite element method for FGMs.

There are many properties which can be modified in graded materials; including, but not limited to, elastic modulus, Poisson's ratio, fiber volume fraction, coefficient of thermal expansion, diffusivity coefficient, thermal conductivity, and density (Ilschner 1996). For many applications; however, the most common variation is in the elastic modulus and Poisson's ratio. In the following section, the variation of the elastic modulus and Poisson's ratio is demonstrated, and its finite element implementation is outlined. In Section 2.4, a formulation is presented which demonstrates the spatial variation of fiber volume fraction.

2.1.1 Implementation of Varying Elastic Modulus and Poisson's Ratio

In the finite element setting, the elastic modulus and Poisson's ratio are expressed in the constitutive matrix, **D**, relating stresses to strains:

$$\boldsymbol{\sigma} = \mathbf{D}\boldsymbol{\varepsilon} \tag{1}$$

where

$$\mathbf{D} = \frac{E}{1-v^2}\begin{bmatrix} 1 & v & 0 \\ v & 1 & 0 \\ 0 & 0 & \frac{1-v}{2} \end{bmatrix} \quad \text{or} \quad \mathbf{D} = \frac{E}{(1+v)(1-2v)}\begin{bmatrix} 1-v & v & 0 \\ v & 1-v & 0 \\ 0 & 0 & \frac{1-2v}{2} \end{bmatrix} \tag{2}$$

for plane stress or plane strain problems, respectively.

In the standard finite element method, the elastic modulus and Poisson's ratio are constants, but in isoparametric graded finite elements, these properties continuously vary. Thus, instead of the **D** matrix, being constant, it is now a function of location, **D**(***x***), and can be expressed as:

$$\mathbf{D}(\boldsymbol{x}) = \frac{E(\boldsymbol{x})}{1-v(\boldsymbol{x})^2}\begin{bmatrix} 1 & v(\boldsymbol{x}) & 0 \\ v(\boldsymbol{x}) & 1 & 0 \\ 0 & 0 & \frac{1-v(\boldsymbol{x})}{2} \end{bmatrix} \tag{3}$$

or

$$\mathbf{D}(\boldsymbol{x}) = \frac{E(\boldsymbol{x})}{\left[1+v(\boldsymbol{x})\right]\left[1-2v(\boldsymbol{x})\right]}\begin{bmatrix} 1-v(\boldsymbol{x}) & v(\boldsymbol{x}) & 0 \\ v(\boldsymbol{x}) & 1-v(\boldsymbol{x}) & 0 \\ 0 & 0 & \frac{1-2v(\boldsymbol{x})}{2} \end{bmatrix} \tag{4}$$

for plane stress or plain strain problems, respectively.

Material properties, *E*(***x***) and *v*(***x***), still need to be determined for each graded element. Santare and Lambros (2000) proposed sampling the material properties at the Gauss points; while Kim and Paulino (2002) proposed using a generalized isoparametric formulation (GIF). The latter method is the one utilized in this study as it is more natural to the finite element method. The same shape functions used to determine displacements and geometry are used to determine the material parameters, *E* and *v*. For Q4 elements, the standard isoparametric shape functions transform between local and global coordinates:

$$\begin{aligned} N_1(\xi,\eta) &= \left(\frac{1}{4}\right)(1-\xi)(1-\eta) \qquad & N_2(\xi,\eta) &= \left(\frac{1}{4}\right)(1+\xi)(1-\eta) \\ N_3(\xi,\eta) &= \left(\frac{1}{4}\right)(1+\xi)(1+\eta) \qquad & N_4(\xi,\eta) &= \left(\frac{1}{4}\right)(1-\xi)(1+\eta) \end{aligned} \tag{5}$$

where

$$-1 \le \xi \le 1 \qquad \text{and} \qquad -1 \le \eta \le 1 \tag{6}$$

and

$$x = \sum_{i=1}^{m} N_i x_i \qquad \text{and} \qquad y = \sum_{i=1}^{m} N_i y_i \tag{7}$$

Generalizing this concept, we can then extrapolate to get the Young's modulus $E(\boldsymbol{x})$ and Poisson's ratio $v(\boldsymbol{x})$

$$E(\boldsymbol{x}) = \sum_{i=1}^{m} N_i E_i \qquad \text{and} \qquad \mathrm{v}(\boldsymbol{x}) = \sum_{i=1}^{m} N_i v_i \tag{8}$$

respectively, as illustrated in Figure 2.1.

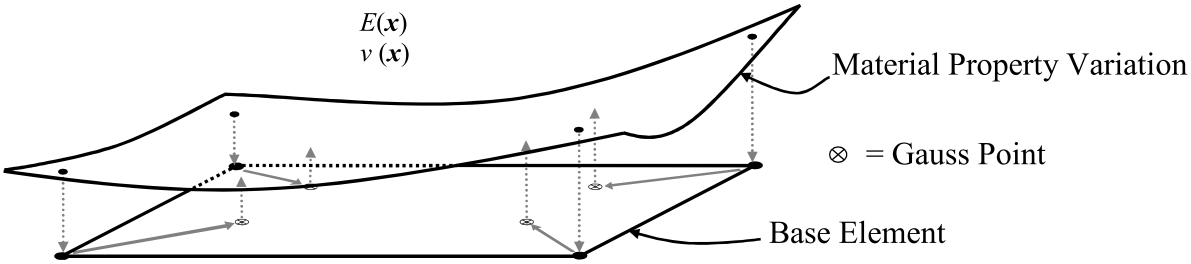

Figure 2.1: Generalized isoparametric formulation for isotropic FGMs.

This framework allows for easy implementation in existing finite element programs, in that the isoparametric structure is already active, and just needs slight modification to account for the variation of material properties.

2.2 Finite Element Implementation of Cohesive Elements

Implementation of cohesive elements into a standard finite element setting can be done with relative ease, and is one of the main reasons for its popularity. The standard finite element formulation can be described mathematically, using the principle of virtual work, as:

$$dW_{int} = dW_{ext} \tag{9}$$

$$\int_{\Omega} \delta\varepsilon^{T} \boldsymbol{\sigma} d\Omega = \int_{\Gamma} \delta u^{T} \mathbf{P} d\Gamma \tag{10}$$

where $\delta\varepsilon$ and $\boldsymbol{\sigma}$ are the virtual strain and Cauchy stress, respectively, in the domain Ω; and δu and $\mathbf{P}$ are the virtual work and external traction vector, respectively, on the boundary of the domain Γ. Using the Galerkin method, the standard finite element formulation can be represented as:

$$\left[\int_{\Omega} \mathbf{B}^T \mathbf{D} \mathbf{B} d\Omega\right] \mathbf{u} = \int_{\Gamma} \mathbf{P} d\Gamma \tag{11}$$

where **B** is the strain displacement matrix, and **D** is the constitutive (material tangential) matrix. The part in brackets is commonly referred to as the stiffness matrix **K**, and the right hand side is commonly referred to as the external force vector **F**, leaving the well-known formulation:

$$\mathbf{K}\mathbf{u} = \mathbf{F} \tag{12}$$

When including cohesive elements in the formulation, the internal work (Equation 9) needs to be updated to include the component caused by their traction-separation relationship. The resulting formulation is as follows:

$$\int_{\Omega} \delta\varepsilon^T \boldsymbol{\sigma} d\Omega + \int_{\Gamma_{cr}} \delta w^T \mathbf{T} d\Gamma_{cr} = \int_{\Gamma} \delta u^T \mathbf{P} d\Gamma \tag{13}$$

where δw and **T** are the crack opening displacement and corresponding traction along the cohesive zone, respectively, occurring along the crack line Γ_{cr}. Similar to before, the Galerkin method can be used to determine the standard finite element formulation as:

$$\left[\int_{\Omega} \mathbf{B}^T \mathbf{D} \mathbf{B} d\Omega + \int_{\Gamma_{cr}} \mathbf{N}^T \frac{\partial \mathbf{T}}{\partial \boldsymbol{w}} \mathbf{N} d\Gamma_{cr}\right] \mathbf{u} = \int_{\Gamma} \mathbf{P} d\Gamma \tag{14}$$

where **N** is the shape function matrix, used to interpolate the crack opening displacement into nodal displacements.

2.3 Plain Concrete Cohesive Zone Model

Historically, accurately modeling the fracture of plain concrete has been a difficult problem. There have been many proposed cohesive models over the years, each having their own pros and cons. One of the most frequently used models incorporates a bilinear traction separation relationship to model the softening of concrete, commonly referred to as the bilinear softening model.

The bilinear traction separation relationship (Figure 2.2) can be defined from three, experimentally determined, input parameters: initial fracture energy (G_f), total fracture energy (G_F), and tensile (cohesive) strength (f_t').

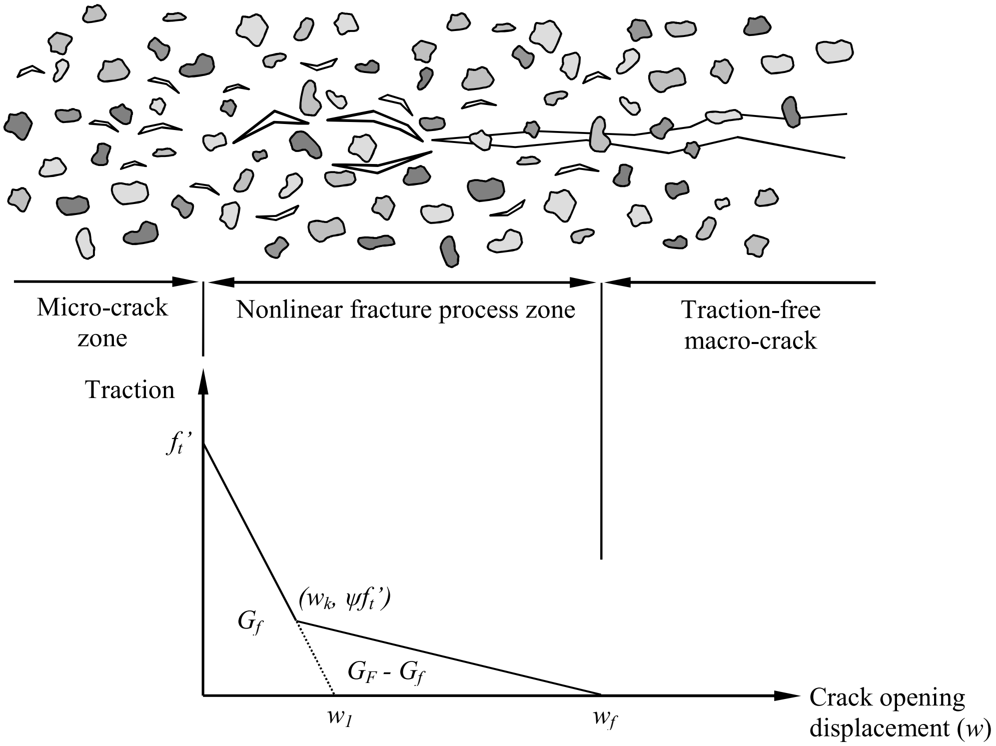

Figure 2.2: Bilinear traction separation relationship for plain concrete.

To implement this relationship into the standard finite element method, the traction vector along the crack surface and the tangential (Jacobian) matrix need to be defined for each cohesive element. The traction vector, **T**, used to calculate the right-hand side (RHS) vector in Equation (13), is represented as:

$$\mathbf{T} = \left\{ T_{s1} \quad T_{s2} \quad T_n \right\}^{\mathrm{T}} \tag{15}$$

where

$$T_{si} = \left(\frac{f_t'}{w_{cr}} \right) w_{si} \tag{16}$$

and

$$T_n = \begin{Bmatrix} \left(\dfrac{f_t'}{w_{cr}} \right) w_n & \left(0 \le w_n \le w_{cr} \right) \\ \left(\dfrac{w_1 - w_n}{w_1 - w_{cr}} \right) f_t' & \left(w_{cr} < w_n \le w_x \right) \\ \left(\dfrac{w_f - w_n}{w_f - w_x} \right) f_t' \cdot \psi & \left(w_x < w_n \le w_f \right) \\ 0 & \left(w_f < w_n \right) \end{Bmatrix} \tag{17}$$

In order to determine the cohesive element's contribution to the stiffness matrix (see Equation 14) the tangential (Jacobian) matrix is determined as:

$$\frac{\partial \mathbf{T}}{\partial \boldsymbol{w}} = \begin{bmatrix} \dfrac{\partial T_{s1}}{\partial w_{s1}} & \dfrac{\partial T_{s1}}{\partial w_{s2}} & \dfrac{\partial T_{s1}}{\partial w_{n}} \\ \dfrac{\partial T_{s2}}{\partial w_{s1}} & \dfrac{\partial T_{s2}}{\partial w_{s2}} & \dfrac{\partial T_{s2}}{\partial w_{n}} \\ \dfrac{\partial T_{n}}{\partial w_{s1}} & \dfrac{\partial T_{n}}{\partial w_{s2}} & \dfrac{\partial T_{n}}{\partial w_{n}} \end{bmatrix} \tag{18}$$

where

$$\frac{\partial T_n}{\partial w_n} = \left\{ \begin{array}{ll} \left(\dfrac{f_t'}{w_{cr}}\right) & \left(0 \le w_n \le w_{cr}\right) \\ \left(\dfrac{-f_t'}{w_1 - w_{cr}}\right) & \left(w_{cr} < w_n \le w_x\right) \\ \left(\dfrac{-f_t'}{w_f - w_x}\right)\cdot\psi & \left(w_x < w_n \le w_f\right) \\ 0 & \left(w_f < w_n\right) \end{array} \right\} \tag{19}$$

$$\frac{\partial T_{s1}}{\partial w_{s1}} = \frac{\partial T_{s2}}{\partial w_{s2}} = \left(\frac{f_t'}{w_{cr}}\right) \tag{20}$$

$$\frac{\partial T_{s1}}{\partial w_{s2}} = \frac{\partial T_{s1}}{\partial w_{n}} = \frac{\partial T_{s2}}{\partial w_{s1}} = \frac{\partial T_{s2}}{\partial w_{n}} = \frac{\partial T_{n}}{\partial w_{s1}} = \frac{\partial T_{n}}{\partial w_{s2}} = 0 \tag{21}$$

2.4 Fiber Reinforced Concrete Cohesive Zone Model

A common method of improving the performance of plain concrete structures is to add steel fibers. The volume of fibers can be distributed homogeneously throughout the concrete, or it can be spatially distributed throughout the structure to provide improved, localized functionality where needed. The addition of steel fibers has been shown to increase the impact strength and toughness of concrete (Nataraja et al. 2000). Banthia (1997) shows that the addition of steel fibers inhibits crack growth and reduces crack opening displacement at large loads.

To accurately model the effect of fibers in the concrete mixture, the traction-separation relationship needs to be modified. Without fibers present, the traction separation relationship consists of a bilinear softening curve. Park et al. (2010) propose a tri-linear softening curve which would better capture the effect of the fibers. The tri-linear model relies on six input parameters which can be determined experimentally: initial fracture energy (G_f), total fracture energy of plain concrete (G_F), total fracture energy of fiber reinforced concrete (G_{FRC}), tensile strength (f_t'), critical crack tip opening displacement ($CTOD_c$), and fiber length (L_f). These six parameters define the traction-separation relationship illustrated in Figure 2.3.

To implement this relationship into the standard finite element method, the traction vector along the crack surface and the tangential (Jacobian) matrix needs to be defined for each cohesive element. The traction vector, **T**, used to calculate the RHS vector in Equation (13), is represented as in expression (15), where:

$$T_{si} = \left(\frac{f_t'}{w_{cr}}\right) w_{si} \tag{22}$$

$$T_n = \left\{ \begin{array}{ll} \left(\frac{f_t'}{w_{cr}}\right) w_n & \left(0 \le w_n \le w_{cr}\right) \\ \left(\frac{w_1 - w_n}{w_1 - w_{cr}}\right) f_t' & \left(w_{cr} < w_n \le w_{k1}\right) \\ \left(\frac{w_2 - w_n}{w_2 - w_{k1}}\right) f_t' \cdot \psi_1 & \left(w_{k1} < w_n \le w_{k2}\right) \\ \left(\frac{w_f - w_n}{w_f - w_{k2}}\right) f_t' \cdot \psi_2 & \left(w_{k2} < w_n \le w_f\right) \\ 0 & \left(w_f < w_n\right) \end{array} \right\} \tag{23}$$

In order to determine the cohesive element contribution to the stiffness matrix (see Equation 14) the components of the tangential (Jacobian) matrix, as defined in expression (18), are:

$$\frac{\partial T_n}{\partial w_n} = \left\{ \begin{array}{ll} \left(\frac{f_t'}{w_{cr}}\right) & \left(0 \le w_n \le w_{cr}\right) \\ \left(\frac{-f_t'}{w_1 - w_{cr}}\right) & \left(w_{cr} < w_n \le w_{k1}\right) \\ \left(\frac{-f_t'}{w_2 - w_{k1}}\right) \cdot \psi_1 & \left(w_{k1} < w_n \le w_{k2}\right) \\ \left(\frac{-f_t'}{w_f - w_{k2}}\right) \cdot \psi_2 & \left(w_{k2} < w_n \le w_f\right) \\ 0 & \left(w_f < w_n\right) \end{array} \right\} \tag{24}$$

$$\frac{\partial T_{s1}}{\partial w_{s1}} = \frac{\partial T_{s2}}{\partial w_{s2}} = \left(\frac{f_t'}{w_{cr}}\right) \tag{25}$$

$$\frac{\partial T_{s1}}{\partial w_{s2}} = \frac{\partial T_{s1}}{\partial w_n} = \frac{\partial T_{s2}}{\partial w_{s1}} = \frac{\partial T_{s2}}{\partial w_n} = \frac{\partial T_n}{\partial w_{s1}} = \frac{\partial T_n}{\partial w_{s2}} = 0 \tag{26}$$

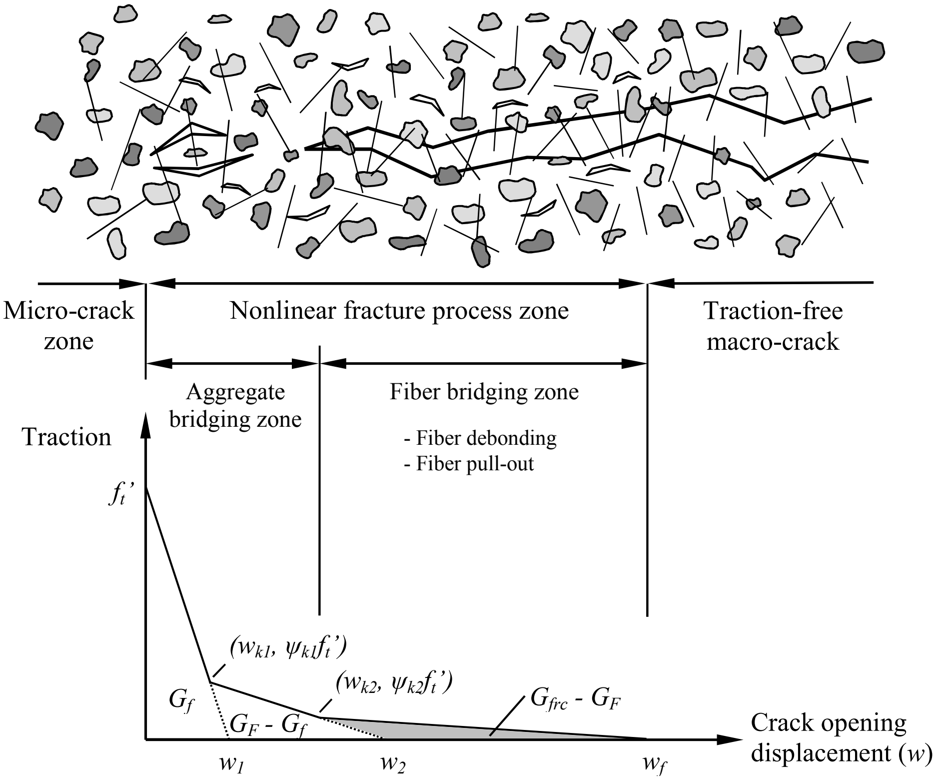

Figure 2.3: Traction separation relationship for fiber reinforced concrete (FRC).

2.5 Functionally Graded Cohesive Zone Model

When pouring layered slabs in the field, the various layers undergo some mixing during consolidation. This mixing often causes what is known as a transition zone, where the properties of the material may change. To accurately model this property transition, functionally graded cohesive zone elements (FGCZEs) can be utilized in the computational model.

In this study, the computational model for fiber reinforced concrete is extended to allow for spatial variation of fiber volume fraction. The resulting cohesive zone model remains tri-linear (see Figure 2.4) but, the total fracture energy of FRC is a spatially dependent value, $G_{FRC}(\boldsymbol{x})$. The variation of total fracture energy of FRC in space causes the second kink point in the tri-linear softening region to also be spatially dependent, through the relationship:

$$\psi_{k2}\left(\boldsymbol{x}\right)=\frac{2\left(G_{FRC}\left(\boldsymbol{x}\right)-G_{F}\right)}{f_{t}^{'}\left(w_{f}-w_{2}\right)} \tag{27}$$

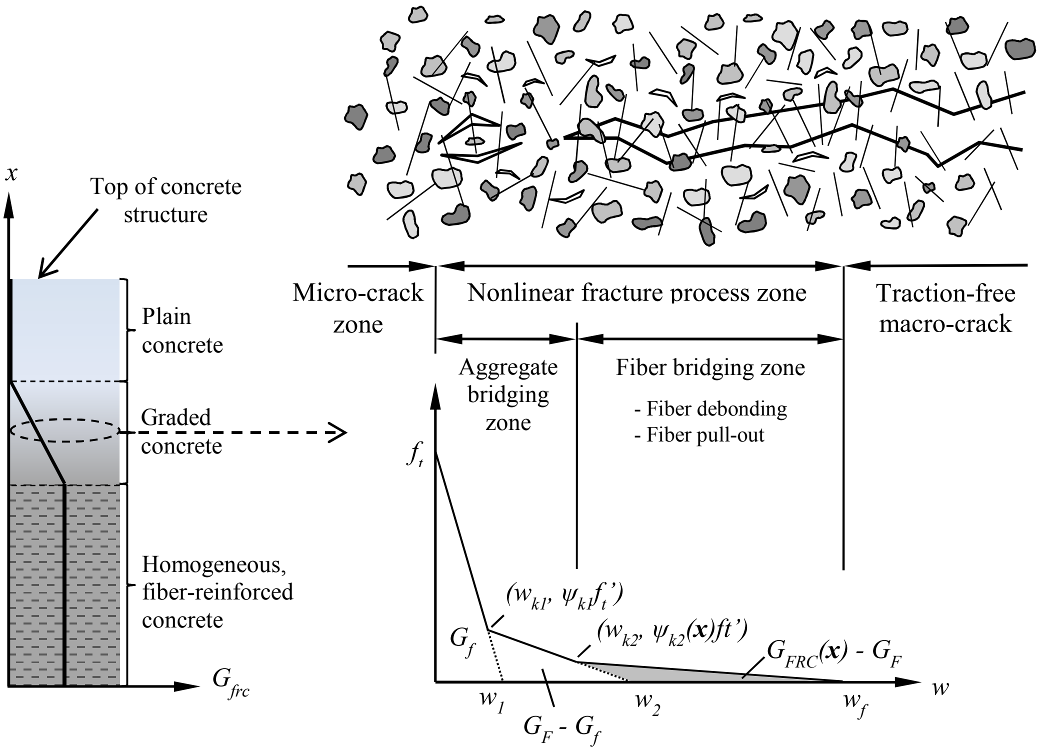

Figure 2.4: Traction separation relationship for spatially varied FRC.

To update the constitutive model, we use the generalized isoparametric formulation (GIF), proposed by Kim and Paulino (2002), and described in detail in Section 2.1.2. Utilizing this formulation, the total fracture energy of the FRC, can be represented as:

$$G_{FRC}=\sum_{i=1}^{nel}N_{i}G_{FRCi} \tag{28}$$

where *nel* is the number of nodes in the element. Implementing this continuous spatial variation of fiber volume fraction, as opposed to homogeneously stepped elements, avoids the unnecessary stress jumps caused by the discontinuity in the material, as illustrated in Figure 2.5.

A user defined subroutine (UEL) implementing the above cohesive model in the finite element analysis software ABAQUS can be found in the Appendix 1. The nodal coordinates, displacements, and element properties are input to the UEL, while the residual force vector and the stiffness matrix are output from the UEL (ABAQUS 2002).

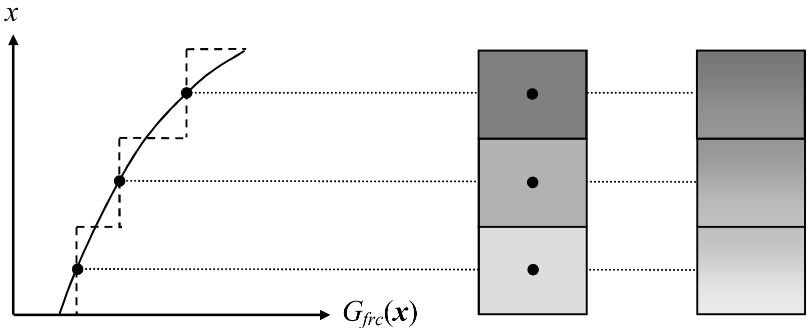

Figure 2.5: Properties of homogeneously stepped elements, and continuously varied elements.

2.6 Code Verification

The above formulations are implemented into a user defined element subroutine (UEL), in ABAQUS, and verified numerically. To verify that the element is producing accurate results, a single element test is used in which a single bulk element and a single cohesive element make up the entire model. A displacement boundary condition is applied to the bulk element, causing the cohesive element (with an initial thickness of zero) to separate and produce tractions.

For the bilinear cohesive element code verification, an initial fracture energy of 35N/m, a total fracture energy for plain concrete of 99.2N/m, and a tensile strength of 3.213MPa are used. The model and the results of the simulation are shown in Figure 2.6.

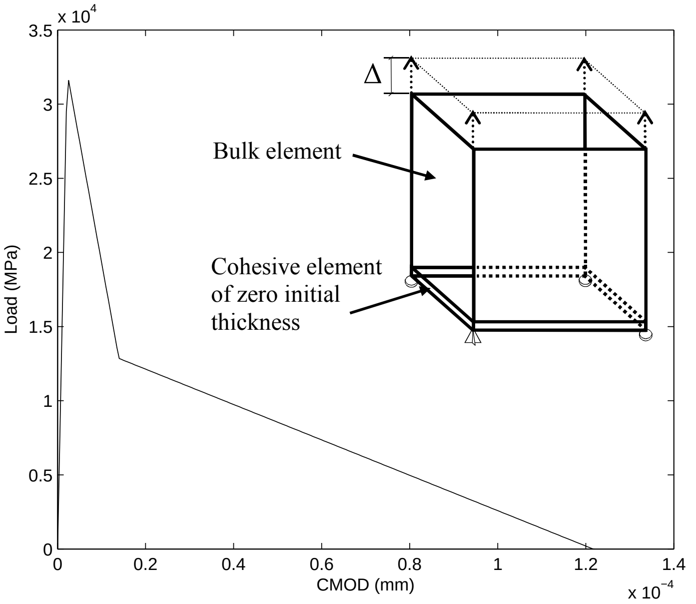

Figure 2.6: Single bulk element and single cohesive element, and corresponding traction-separation relationship (used for code verification) for plain concrete.

The model is able to capture the bilinear softening behaviour of the cohesive interaction diagram, with a kink point located at $\left(w_k, f_t'\right)$ as determined by Park et al. (2008), where:

$$w_k = CTOD_c \tag{29}$$

$$\psi = 1 - \frac{CTOD_c f_t'}{2G_f} \tag{30}$$

For the FRC code verification, the following properties are used: initial fracture energy of 100N/m, total fracture energy for plain concrete of 200N/m, total fracture energy of FRC of 220N/m, tensile strength of 4.15MPa, critical crack tip opening displacement of 0.0329m, and fiber length of 10mm. The model and the results of the simulation are shown in Figure 2.7.

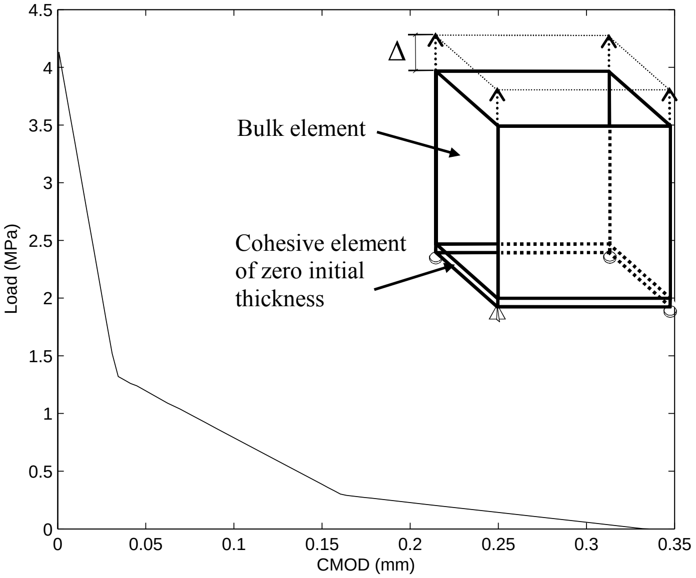

Figure 2.7: Single bulk element and single cohesive element, and corresponding traction-separation relationship (used for code verification) for FRC.

For the spatially varied FGCZE verification, a series of simulations are considered. To accurately determine whether the code is implemented correctly, a column of elements is modeled, and the total fracture energy is varied along the height of the column, as illustrated in Figure 2.8. A single element in the column is picked, and the resulting load-displacement relationship is plotted in Figure 2.9.

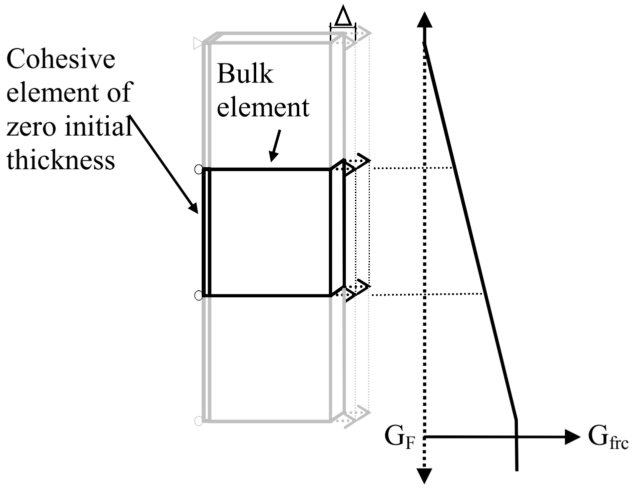

Figure 2.8: Spatial variation in total fracture energy of FRC.

The simulations are performed with the following properties: initial fracture energy of 100N/m, total fracture energy for plain concrete of 200N/m, tensile strength of 4.15MPa, critical crack tip opening displacement of 0.0329m, fiber length of 10mm, minimum total fracture energy of FRC of 200N/m, and maximum total fracture energy of 240N/m. As illustrated in Figure 2.9, as the total fracture energy of FRC reduces, the second kink point in the softening region approaches zero. When it reduces to the total fracture energy of plain concrete, the bilinear softening behaviour is recovered.

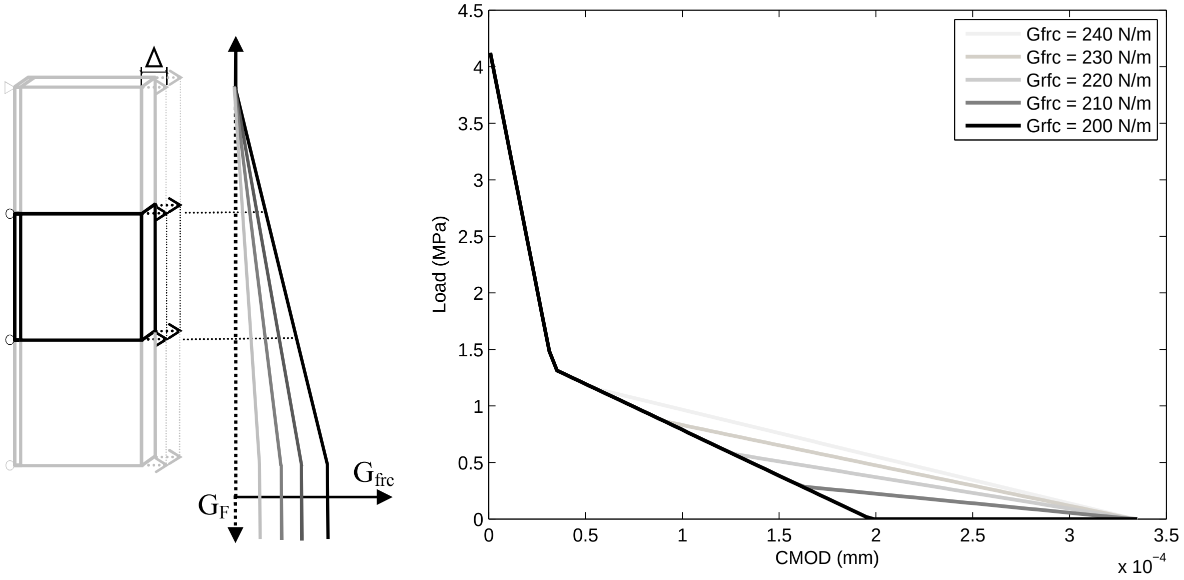

(a) (b)

Figure 2.9: (a) Variation of total fracture energy of FRC with depth (b) Traction-separation relationship (used for code verification) for functionally graded FRC.

CHAPTER 3

DISK-SHAPED COMPACT TENSION TEST FOR FRACTURE OF CONCRETE

Currently there are many tests utilized to determine the mode I fracture properties of concrete; such as, the single edge notched beam (SENB), and wedge split test (Bažant 2002a). These tests are well suited to experimental testing and provide reliable results, but rely on geometries which are difficult to obtain from in-situ concrete in the field. Thus, there is a demand to develop a test as reliable and accurate as the above two, but which uses a specimen geometry that may easily be extracted from existing structures.

There exists technology to extract cylindrical cores from in-situ concrete at relative ease. Therefore, there would be an obvious advantage if these cores could be turned into sample specimens that would allow determination of the fracture properties of concrete. The resulting, proposed specimen geometry is similar to one that is used in the asphalt industry (ASTM D7313), and is herein referred to as the disk-shaped compact tension (DCT) specimen. This Chapter outlines the specimen geometry in section 3.1; describes the determination of the geometric correction factors in section 3.2; summarizes the inputs to the cohesive zone model for the numerical analysis in section 3.3; compares the experimental results with the numerical results in section 3.4; and finally determines the effect of various parameters on the numerical analysis in section 3.5.

3.1 DCT Specimen Geometry

Tada et al. (2000) developed geometric factors for the geometry shown in Figure 3.1. They developed correction factors for the stress intensity factor (K_I), the opening displacement at the load line (d_1) and the crack mouth opening displacement (d_2). This geometry is used in this study, in order to take advantage of the existing geometric factors and analysis (Newman 1979, 1981).

$$K_I(A) = \bar{\sigma}\sqrt{W}F(A) \tag{31}$$

$$F(A) = \frac{(2+A)(0.76+4.8A-11.58A^2+11.43A^3-4.08A^4)}{(1-A)^{3/2}} \tag{32}$$

$$\bar{\sigma} = \frac{P}{WB} \qquad A = \frac{a}{W} \tag{33}$$

$$d_1(A) = \frac{\bar{\sigma}W}{E'} V_1(A) \tag{34}$$

$$V_1(A) = \exp\left(1.742 - 0.495A + 14.71A^2 - 22.06A^3 + 14.44A^4\right) \tag{35}$$

$$d_2(A) = \frac{\bar{\sigma}W}{E'} V_2(A) \tag{36}$$

$$V_2(A) = \exp\left(0.26 + 5.381A + 2.105A^2 - 8.853A^3 + 9.122A^4\right) \tag{37}$$

The critical crack tip opening displacement is a required parameter to determine the softening behaviour of the cohesive model. Thus, there is a need for an additional displacement geometric factor at the tip of the initial notch.

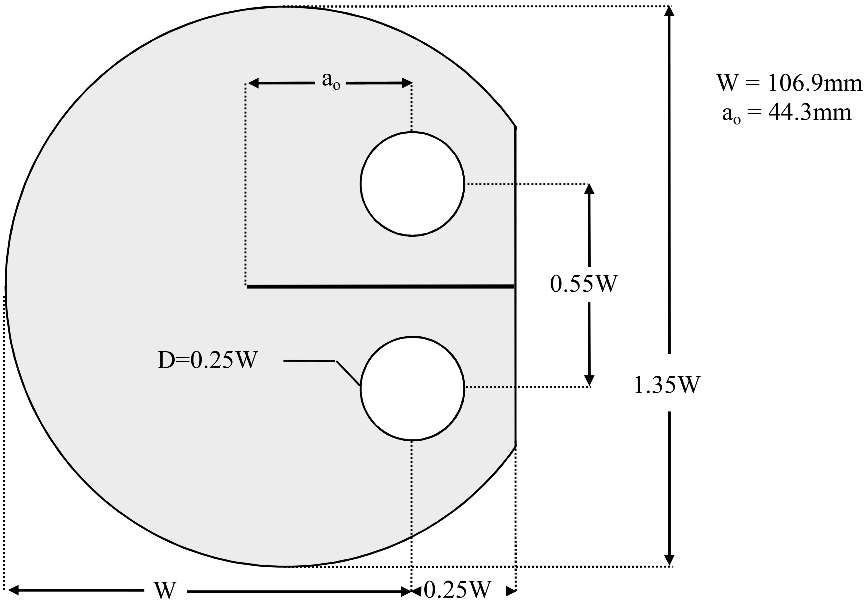

Figure 3.1: DCT specimen geometry.

3.2 Geometric Correction Factor for CTOD

A geometric factor for the crack opening displacement at the notch tip is developed because one is not currently available in the literature. A finite element analysis of the specimen is performed to obtain the required geometric factor. To conduct the analysis, six different models are developed with varying notch depths. A summary of the data for each model is listed in Table 3.1.

Table 3.1: Notch depths for geometric factor analysis.

Model	W [mm]	a [mm]	*A*
1	106.9	96.3	0.90
2	106.9	81.6	0.76
3	106.9	69.7	0.65
4	106.9	57.1	0.53
5	106.9	44.5	0.42
6	106.9	33.3	0.31

The finite element model consists of eight node, quadrilateral (Q8) elements with a radial mesh at the notch tip. Figures 3.3a and 3.3b show the global mesh and the biased radial mesh towards the crack tip, respectively. The elements at the crack tip are collapsed Q8 elements with an average length of 0.03 mm and nodes at the quarter points, see Figure 3.2.

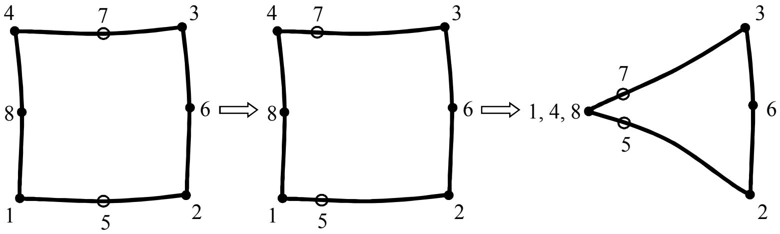

Figure 3.2: Collapsed Q8 elements at crack tip

The quarter point elements enable the model to accurately represent the singular stress field at the crack front. In order to validate the model, to ensure that the results are consistent with the analytical solution, the geometric correction factors at the load line and CMOD are developed and compared with the analytical solution.

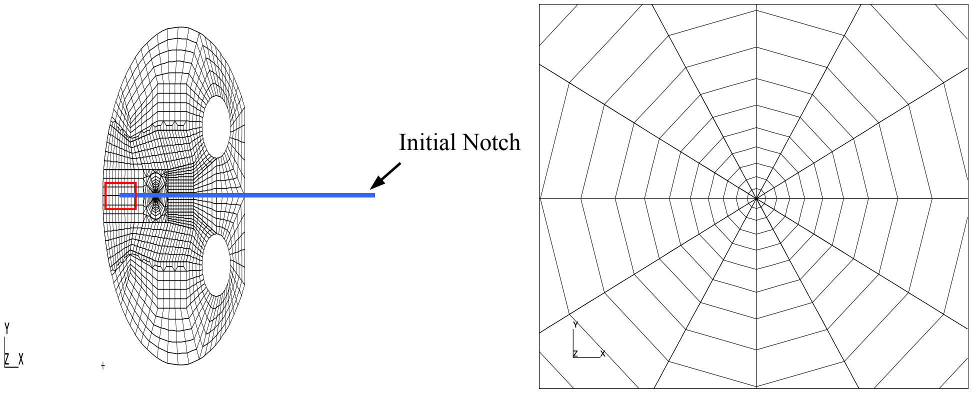

(a) (b)

Figure 3.3: Example DCT finite element mesh: (a) Global mesh, (b) Biased radial mesh towards crack tip.

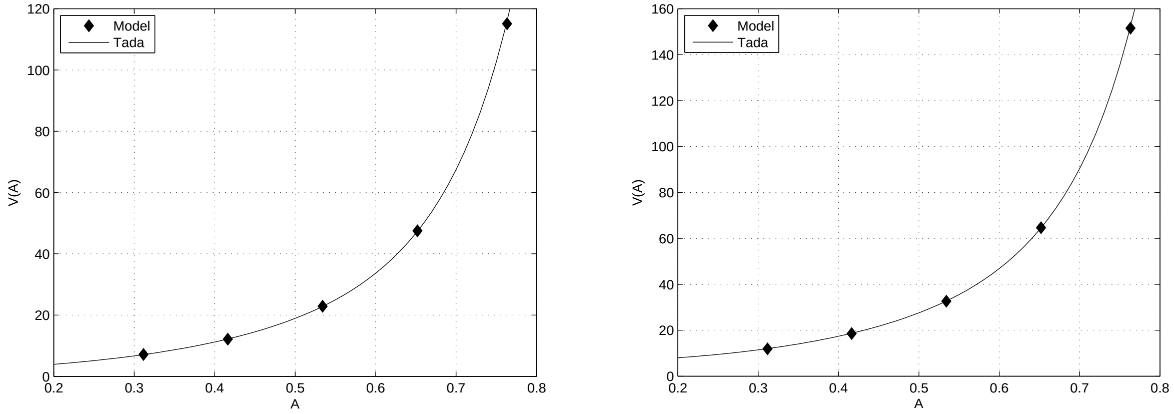

(a) (b)

Figure 3.4: Geometric factor for a) load line displacement b) CMOD.

As illustrated in Figure 3.4, the model is able to closely predict the values obtained by Tada et al. (2000). Table 3.2 shows the exact values of the various factors at the computed points, for plane strain conditions, P = 10,000kN, W = 106.9mm, B = 50.7mm, E = 30GPa, and v = 0.3. The model is able to predict the analytical solution to a reasonable degree of accuracy, so the geometric factor at the initial notch tip (~71mm from the flat face) can be developed with some confidence.

Table 3.2: Comparison between analytical and computational geometric factors.

	A	Tada et al.	FE Model	Difference [%]
$d_1(A)$	0.31	7.090567	7.130769	0.567
	0.42	12.18321	12.13516	-0.394
	0.53	22.83253	22.86923	0.161
	0.65	47.37218	47.50549	0.282
	0.76	115.98158	115.08791	-0.771
$d_2(A)$	0.31	11.99341	11.90769	-0.715
	0.42	18.67699	18.54066	-0.730
	0.53	32.72304	32.66374	-0.181
	0.65	64.57280	64.61538	0.066
	0.76	152.33718	151.54945	-0.517

The newly derived expression for the CTOD geometric correction factor is given in expression (39) and shown graphically in Figure 3.5.

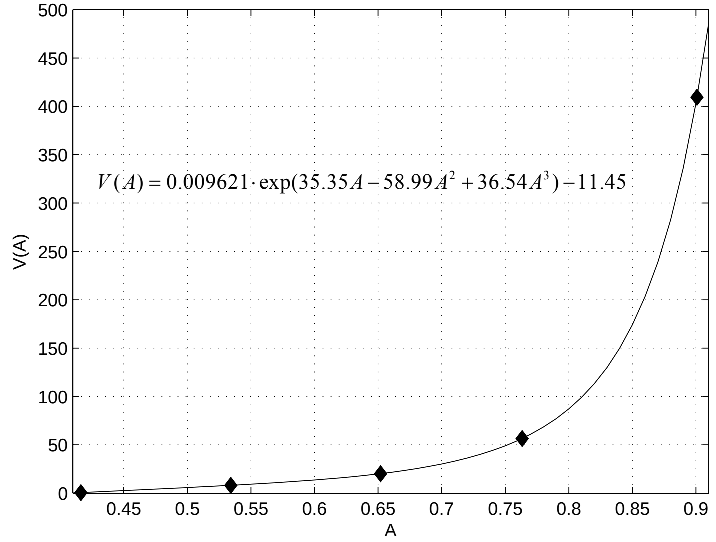

Figure 3.5: Geometric factor for CTOD.

$$CTOD_c(A) = \frac{\overline{\sigma} W V_{CTOD}(A)}{E} \tag{38}$$

$$V_{CTOD}(A) = 0.009621 \cdot \exp(35.35A - 58.99A^2 + 36.54A^3) - 11.45 \tag{39}$$

The above formulation for the $CTOD_c$ is valid in a range $0.41 < A < 0.9$. The initial notch tip is located at around 71mm from the flat face of the specimen ($a_o = 44.3$mm); the computed V_{CTOD} is not applicable for any notch depth smaller than this.

3.3 Inputs to Cohesive Zone Model

Previous work has suggested that a cohesive zone model with bilinear softening can adequately describe the fracture behaviour of concrete (Petersson 1981, Gustafsson and Hillerborg 1985, Wittmann et al. 1988, Guinea et al. 1994, and Bažant 2002b, Roesler et al. 2007b, Park et al. 2008). Figure 3.6a shows the finite element mesh used to simulate the mode I fracture of the DCT specimen. Linear elastic elements (Q4) are used throughout the model, except in front of the crack tip (where cohesive elements are used). The cohesive zone model is implemented in commercial software (ABAQUS) as a user-defined subroutine. Cohesive elements are inserted in front of the initial notch tip and along the expected fracture path of the specimen. In order to model the fracture process accurately, the size of the cohesive crack elements is set to 0.7 mm, which is small enough to capture the nonlinear cohesive zone behaviour (Park 2005). The bilinear softening model shown in Figure 3.6b is utilized to idealize the traction-separation relationship in front of the macro-crack tip.

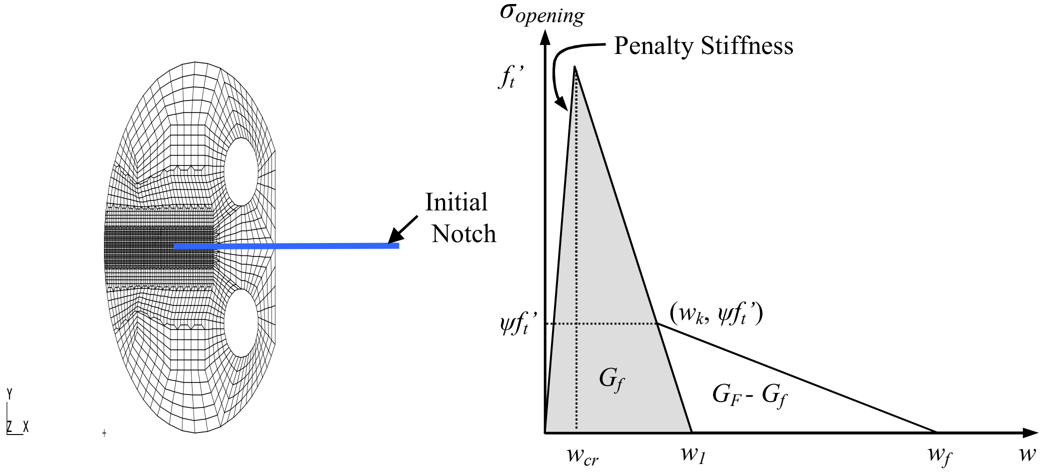

(a) (b)

Figure 3.6: (a) DCT specimen cohesive zone finite element mesh. (b) Cohesive model with bilinear softening (Park et al., 2008).

The experimentally determined input parameters for each material type are listed in Table 3.3.

Table 3.3: Bilinear cohesive model input parameters for limestone and RCA concrete.

Specimen	f_t [MPa]	G_f [N/m]	G_F [N/m]	CTODc [mm]	Ψ [%]	p [w_{cr}/w_f]
Limestone	3.268	26.50	100.1	0.0091	44.3	0.01
RCA	2.455	17.55	92.9	0.0079	45.0	0.01

The model inputs are the cohesive strength (e.g. tensile strength), f_t; the initial and total fracture energies, G_f and G_F respectively; the ratio of the kink point, ψ; and a parameter defining penalty stiffness, p. The tensile strength for the RCA concrete is lowered based on the additional split tensile strength tests, compressive strength results, and ultrasonic pulse velocity tests suggesting the RCA concrete's strength is approximately 25 percent lower than the LCA concrete. The initial fracture energy, G_f, is calculated from Equation (40).

$$G_f = \frac{K_{IC}^2}{E} \tag{40}$$

The kink point is defined (Park et al. 2008) at $(w_k, \psi f_t')$ where:

$$w_k = CTOD_c \tag{41}$$

$$\psi = 1 - \frac{CTOD_c f_t'}{2G_f} \tag{42}$$

The penalty stiffness is determined from the ratio of the opening displacement at the peak load, w_{cr}, to the final opening displacement, w_f, which is chosen to be equal to 0.01.

3.4 Comparison with Experimental Results

The results of the finite element (FE) simulations are presented in Figures 3.7 and 3.8 for the LCA and RCA concrete. The cohesive zone model produced load versus CMOD curves that fell within the envelope of the experimental curves. There is a minor discrepancy observed between the experimental results and the computational model for the CMOD at the peak load. The experiments on the LCA specimens show an average peak load of 1.39kN occurring at a CMOD of 0.067mm, while the FE model show a peak load of 1.32kN occurring at a CMOD of 0.045mm. The experiments on the RCA specimens show an average peak load of 1.02kN occurring at a CMOD of 0.072mm, while the FE model show a peak load of 1.00kN occurring at a CMOD of 0.039mm.

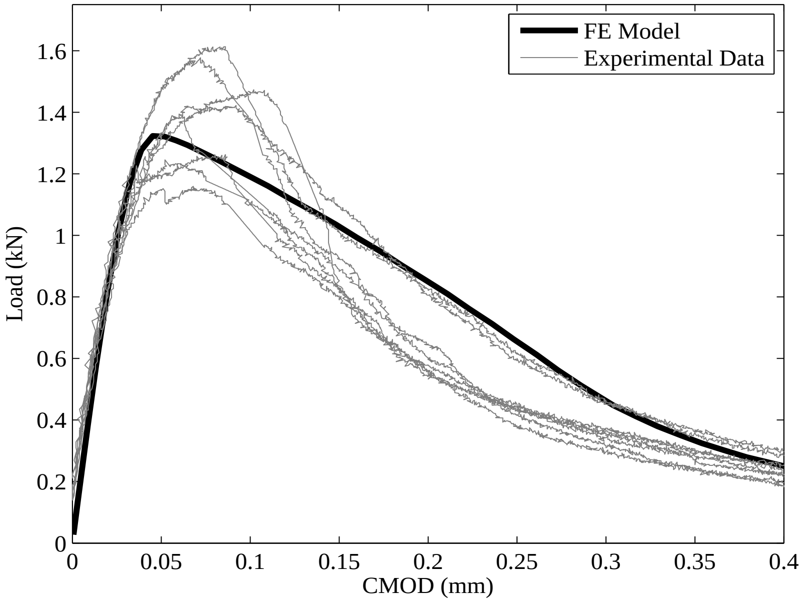

Figure 3.7: DCT experimental and FE model load versus CMOD results for concrete containing limestone coarse aggregate.

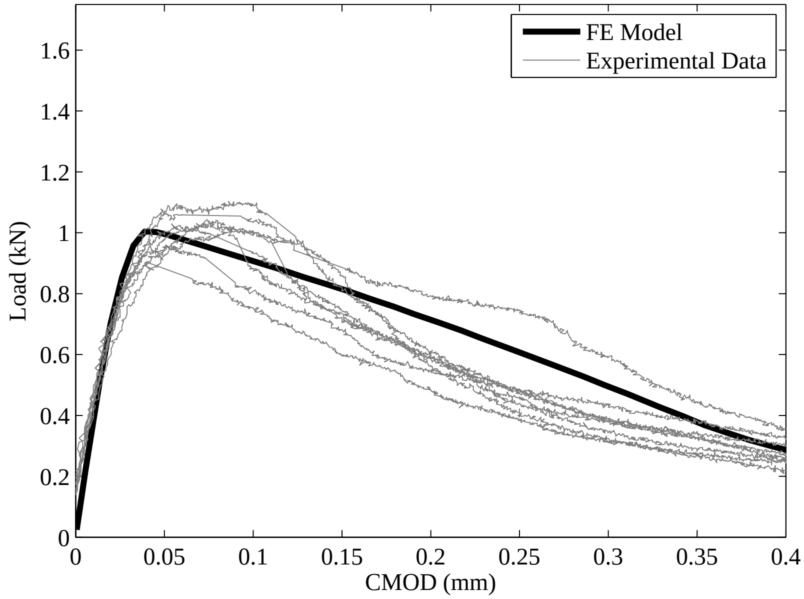

Figure 3.8: DCT experimental and model load versus CMOD results for concrete containing recycled concrete aggregate.

3.5 Parametric Study

To determine the effect of the various inputs to the cohesive model on the bulk response of the DCT specimen, a parametric study is conducted.

Table 3.4: Bilinear cohesive model input parameter ranges for parametric study.

Specimen	Range	f_t [MPa]	G_f [N/m]	G_F [N/m]	Ψ [%]
Limestone	Min.	2.941	20.00	90.0	35.0
	Base	3.268	26.50	100.1	44.3
	Max.	3.595	33.00	110.0	55.0

The parameters of interest include the cohesive strength (f_t), the initial fracture energy (G_f), the total fracture energy (G_F), and the location of the kink point (ψ). The base case is assumed to be that of the limestone specimen shown in Table 3.3. The range of variation for each parameter is listed in Table 3.4. The result of varying each parameter on the bilinear traction-separation relationship is illustrated in Figure 3.9.

As illustrated by Figure 3.9, the variation of each property has a different effect on the cohesive model. Increasing the cohesive strength (f_t) causes the traction free crack to occur at a lower crack opening displacement. It also causes the kink point in the bilinear softening region to occur at a higher strength and lower crack opening displacement. Increasing the initial fracture energy (G_f) also causes the traction free crack to occur at a lower crack opening displacement, but it causes the kink point in the bilinear softening region to occur at a higher strength and larger crack opening displacement. Increasing the total fracture energy (G_F) has no effect on the initial portion of the softening model; its effect is isolated to increasing the traction free crack opening displacement. Finally, increasing the kink point (ψ) has the effect of decreasing the traction free crack opening displacement.

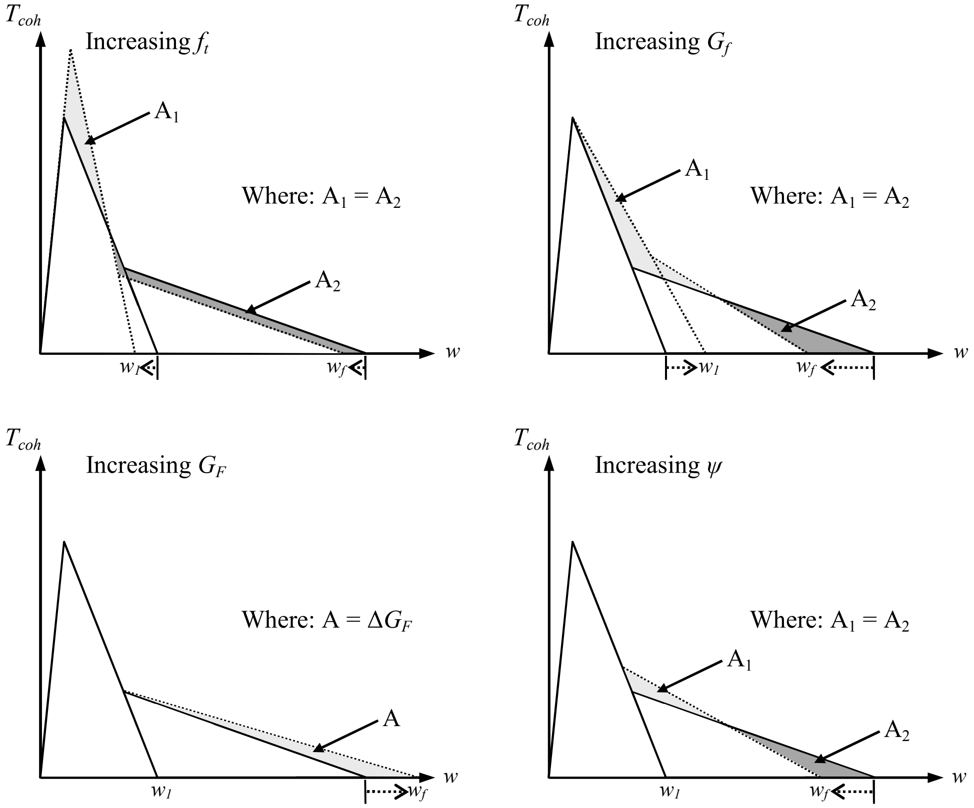

Figure 3.9: Effect of various parameters on the bilinear cohesive traction separation relationship.

When the cohesive strength is varied by 10 percent in each direction, the affect is quite complex, as shown in Figure 3.10. First, the peak load shifts by about 4.7 percent, increasing when the strength is increased, and decreasing when the strength is decreased. Second, the slope of the softening region becomes steeper as the cohesive strength increases. All three of the curves cross in the softening region at a value of about (0.235mm, 705kN).

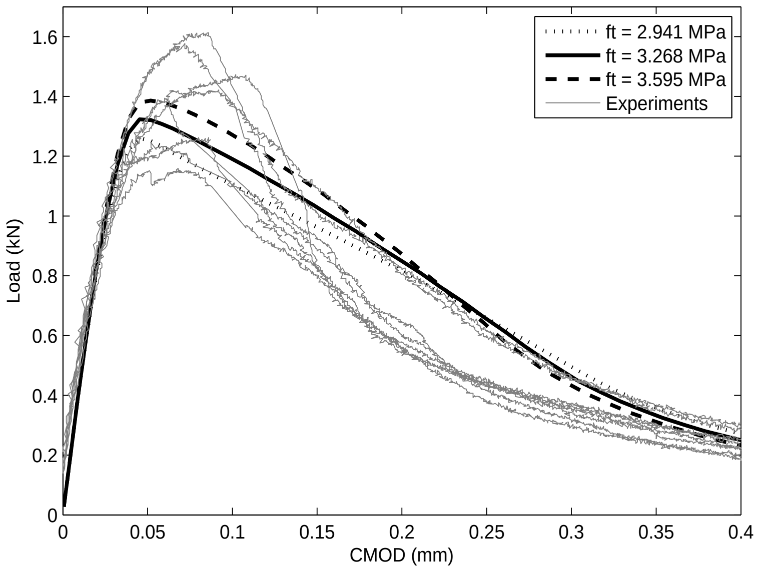

Figure 3.10: Load-CMOD curve with variation of f_t.

For this study, the cohesive strength is chosen as being equal to the rupture strength (measured using a split cylinder test). This is often considered to be an invalid assumption, as there is little evidence supporting the ability to use a global parameter ($f_{rupture}$) to estimate a local parameter (f_t), but it is a simple way of approximating the cohesive strength without having to do an inverse analysis. Thus, the parametric study on the effect of the cohesive strength is quite interesting, as the variation of the cohesive strength shows that for every variation of 0.25Mpa, in the cohesive strength, results in a change in the peak load of only 3.6 percent. This shows that the cohesive strength has very little influence on the response of the specimen, meaning that the rupture strength can be used as a reasonable assumption for the cohesive strength with little effect.

The effect of varying the initial fracture energy is primarily isolated to the initial region of the load-CMOD curve, in particular, at the transition between hardening and softening behaviour. Increasing the initial fracture energy causes the transition between hardening and softening to occur more sharply, as illustrated in Figure 3.11. When the initial fracture energy increases by 25 percent, the peak load increases by about 6 percent (from 1.32kN to 1.40kN). Similarly, when the initial fracture energy decreases by 25 percent, the peak load decreases by about 7 percent (from 1.32kN to 1.23kN). Also, as the initial fracture energy increases, the peak load occurs at a higher CMOD. This also can be explained by observing the bilinear cohesive model in Figure 3.9. As the initial fracture energy increases, the difference between the horizontal axis intercept of the initial descending line (w_1) and the final crack opening width (w_f) decreases, and the peak of the initial fracture energy extends up and to the right.

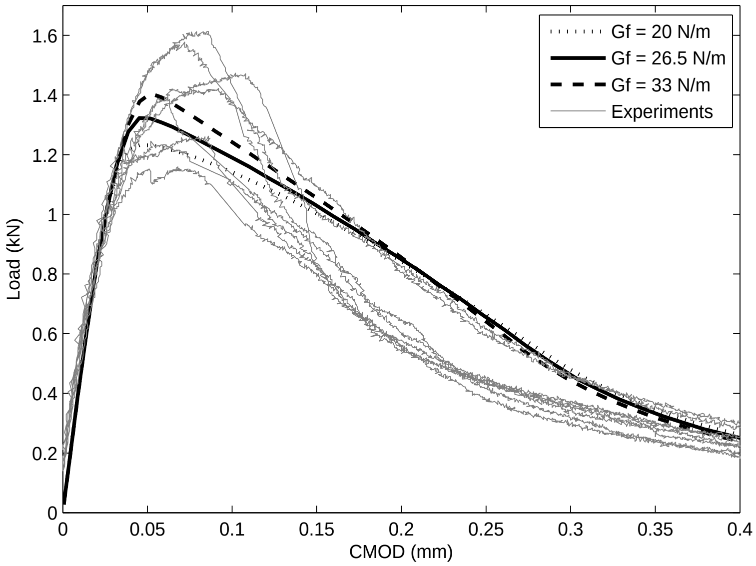

Figure 3.11: Load-CMOD curve with variation of G_f.

Similarly, the variation in total fracture energy, illustrated in Figure 3.12, has little to no effect on the hardening behaviour of the model. The effect is isolated to the softening region, and tends to show an increasing slope with increasing energy. These results are consistent with expectations, as the total fracture energy only affects the post peak traction-separation relationship in the bi-linear cohesive model shown in Figure 3.9. When the fracture energy decreases by 10 percent, the slope of the softening region falls much closer to the mean of the experimental curves. As is noted previously, the softening region is generally overestimated in the modelling process. A possible solution to better correlating the model with the experiments could be to lower the computed total fracture energy.

The results of the variation in the kink point are illustrated in Figure 3.13. When the value of the kink point is reduced by 10 global percent, the resulting softening portion of the Load-CMOD curve becomes more concave. A side effect of the increasing concavity of the softening region is an increasingly sharp transition between the hardening and softening portion of the curve. As the experimental data shows a gradual transition between these two regions, the model is not able to produce optimal results when a lower kink point is used.

When the kink point is raised, the initial portion of the softening curve is convex, and gradually becomes concave near the end of the loading history. This convexity causes the transition between hardening and softening to occur much more gradually, than that with the lower kink points, and moves the peak load to a CMOD much more in line with the experimental average (0.071mm versus 0.072mm).

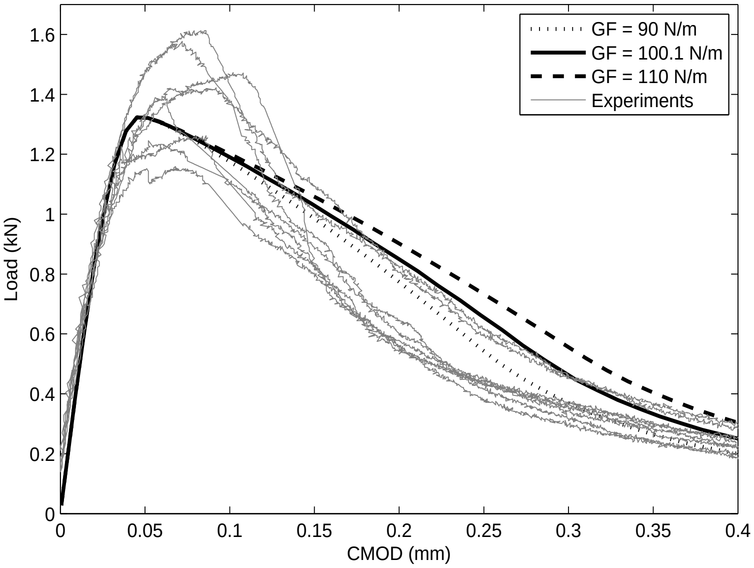

Figure 3.12: Load-CMOD curve with variation of G_F.

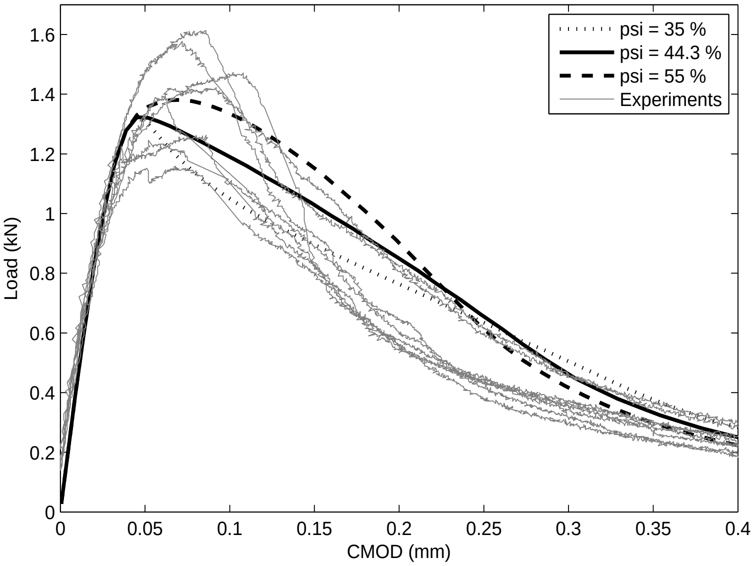

Figure 3.13: Load-CMOD curve with variation of ψ.

CHAPTER 4

THREE-DIMENSIONAL, FUNCTIONALLY GRADED SLABS

In order to determine the failure mechanisms of functionally graded slabs on soil, a numerical study is conducted. The numerical study is modelled after an experimental testing program (a different study) to be done at the Advanced Transportation Research and Engineering Laboratory (ATREL) located in Rantoul, IL. The experimental study will not be completed at the time of publication, thus an essentially numerical approach investigating the behaviour of the slabs is adopted.

There have been many studies conducted on homogeneous, steel fiber reinforced concrete (SFRC) slabs. Barros and Figueiras (1998) study the effect of SFRC slabs on a soil box. They find that SFRC slabs are more ductile and are able to carry a larger peak-load than unreinforced concrete slabs. Khallo and Afshari (2004) conduct similar tests on SFRC slabs, but focus on the effect of the fiber volume fraction in the slabs. They find that increasing the fiber volume fraction does not increase significantly the flexural strength, but does increase the energy absorption capacity of the slabs.

Additional studies have been conducted on the use of sustainable forms of concrete. Many have focused on the inclusion of sustainable forms of reinforcing bars (Barros da S. Santos Neto and La Rovere, 2010; El-Ragaby et al., 2007), but a few have focused on the use of recycled concrete aggregates (Vancura et al., 2009; Zhou et al., 2008; Imamoto et al., 2004). In general, these studies find that, in certain circumstances, sustainable forms of concrete can provide performance very close to that of virgin concrete with limestone aggregates.

Previous studies of functionally graded concrete (FGC) focus primarily on beams (Roesler et al., 2007a; Park et al., 2010; Shen et al., 2008). Each of these studies shows that the use of FGC in commercial applications has promise. The main observation is that the addition of fibers leads to an improved, more ductile softening behaviour. Another common observation is that the fibers close to the initial notch show a greater effect on the response of the beams than those further away. This Chapter outlines the experimental setup in Section 4.1; describes the computational model in Section 4.2; summarizes a study on FGC beams in Section 4.3; outlines a geometric study on the slab model in Section 4.4; summarizes a study on FGC slabs in Section 4.5 and finally determines the effect of various parameters on the numerical analysis in Section 4.6.

4.1 Experimental/Problem Description

The experimental tests are done on 150mm x 1800mm x 1800mm functionally graded slabs. The slabs themselves consist of two layers. The lower layer is 100mm thick while the upper layer is 50mm thick. The initial notch is 50mm deep and extends the length of the slab. There are three different types of concrete chosen for this analysis: concrete with virgin limestone aggregates, concrete with recycled aggregates, and SFRC. The six different combinations chosen for analysis are illustrated in Figure 4.1.

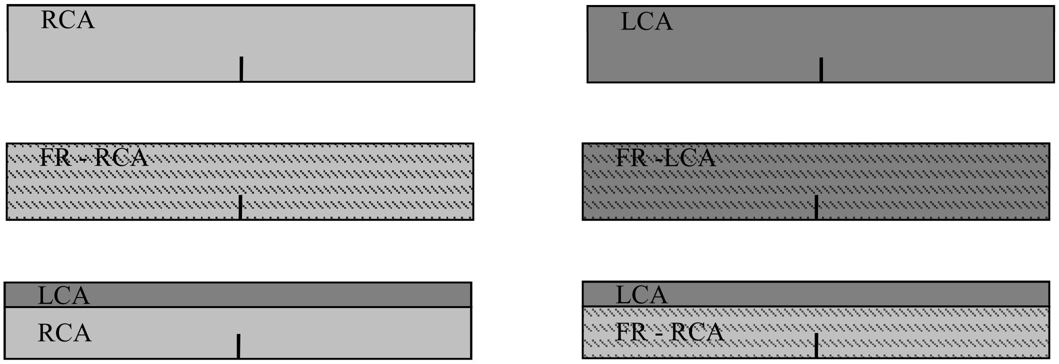

Figure 4.1: Slab combinations investigated. Where: RCA = Recycled Concrete Aggregate; LCA = Limestone Concrete Aggregate; FR = Fiber Reinforced.

The slabs are loaded with a 300mm x 300mm loading plate at the center of one edge of the slab, as shown in Figure 4.2. There are seven Linear Variable Differential Transformer (LVDT) sensors located at the corners and along the edges of the slab to measure displacement at these points, see Figure 4.3a. In addition, there is one strain gauge located at the mouth of the initial notch to measure the crack mouth opening displacement (CMOD).

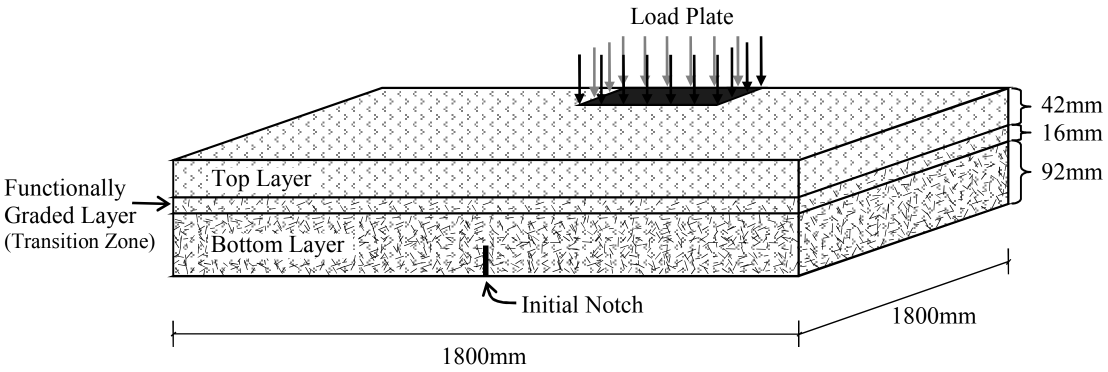

Figure 4.2: Functionally graded slab.

The slabs are loaded on a layered soil bed that consists of: 25mm of sand, 100mm of clay, and 50mm of gravel and water, as illustrated in Figure 4.3b.

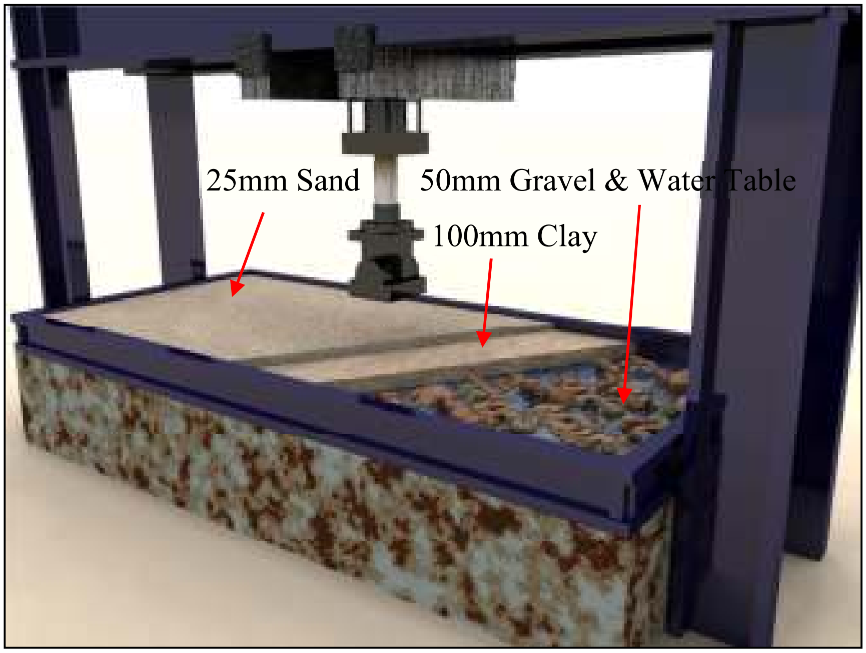

(a)

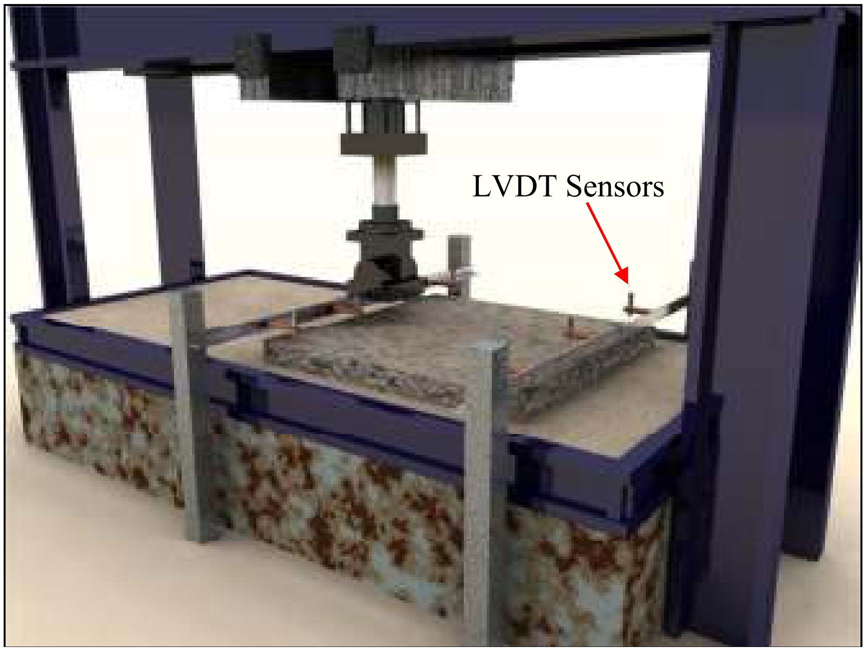

(b)

Figure 4.3: (a) Layers of soil bed (b) Loading apparatus for slab testing (Amirkhanian, 2010).

4.2 Computational Model

The numerical simulations are conducted with user defined elements and user defined materials in the commercial finite element analysis software ABAQUS. The model consists of two distinct components: the slab and the soil.

4.2.1 Slab Model

The bulk of the model is composed of three-dimensional, 8 node, brick elements. These are used to model the homogenous layers of concrete. To model the fracture of the slabs, cohesive zone elements are inserted along the expected fracture path. To model the functionally graded layer (transition zone, as shown in Figure 4.2), isoparametric, functionally graded bulk elements are implemented in a user defined material (UMAT), as described in Section 2.1. The cohesive elements are implemented in user defined elements (UEL's), as described in Chapter 2. In total, 275,220 bulk elements and 28,800 cohesive elements comprise the model of the slab.

The properties of the LCA and RCA concrete are taken from the DCT tests done in Chapter 3. The properties of the FRC are taken from previous studies (Barros and Cruz, 2001; Kazemi et al, 2007; Olivito and Zuccarello, 2009). The properties of the FRC are from tests done on similar types of LCA and RCA concrete to those used in this study. The effect of the FRC properties will be investigated in Section 4.6. A summary of the material properties is listed in Table 4.1.

Table 4.1: Concrete properties.

Specimen	f_t [MPa]	G_f [N/m]	G_F [N/m]	CTODc [mm]	Ψ [%]	p [w_{cr}/w_f]
LCA	3.268	26.50	100.1	0.0091	44.3	0.01
RCA	2.455	17.55	92.9	0.0079	45.0	0.01

4.2.2 Soil Model

In order to idealize the soil, and simplify the model, it is assumed to be homogeneous and is modeled using nonlinear springs with spring stiffness defined in Figure 4.4. The properties of the soil are approximated from a previous study done by Gaedicke (2009). He analyzes homogeneous slabs on two different soils which bear resemblance to the one used in this study. The two soils from his study have stiffness values of 123kPa/mm² and 156kPa/mm², respectively. Gaedicke also determines that the soil has little effect on the response of the slabs, and since (in this study) the relative effect of various concrete properties is what is being investigated, a soil stiffness of 150kPa/mm² is used throughout the simulations. In total, 5,807 vertical spring elements and 5,807 horizontal spring elements comprise the model of the soil.

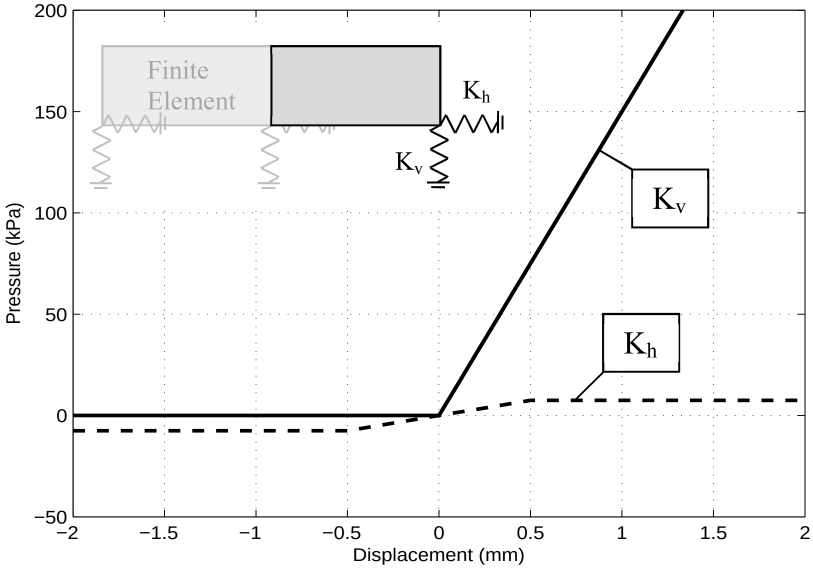

Figure 4.4: Constitutive behaviour of vertical and horizontal springs representing soil.

To verify that the soil stiffness has little effect on the response of the beam, as Gaedicke previously concludes, a simple study is conducted. Two identical beams, resting on a soil box, loaded in a mode I fracture state, are simulated using the two different soil stiffness values of 123kPa/mm² and 156kPa/mm². Figure 4.5 shows that a difference of 27 percent in the soil stiffness only causes a 7 percent difference in the observed peak-loads of the beam.

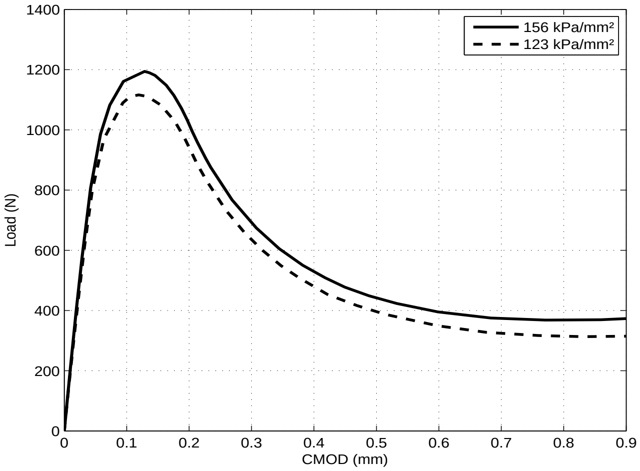

Figure 4.5: Effect of soil stiffness on Load-CMOD curve.

To aid in the affirmation that the nonlinear springs are a suitable substitute for a more complex soil model, a visual comparison of the experimental and virtual simulations is done. Experimentally, it is observed that, shortly after loading, the portion of the slab furthest from the loading plate lifts up, and at the peak-load, only a small portion of the slab is in contact with the soil bed. The numerical model shows similar results. Figure 4.6 shows the displacement of the springs beneath the slab at the peak-load. Clearly, one can see that the slab lifts up and relies only on a small portion of the soil box to provide resistance.

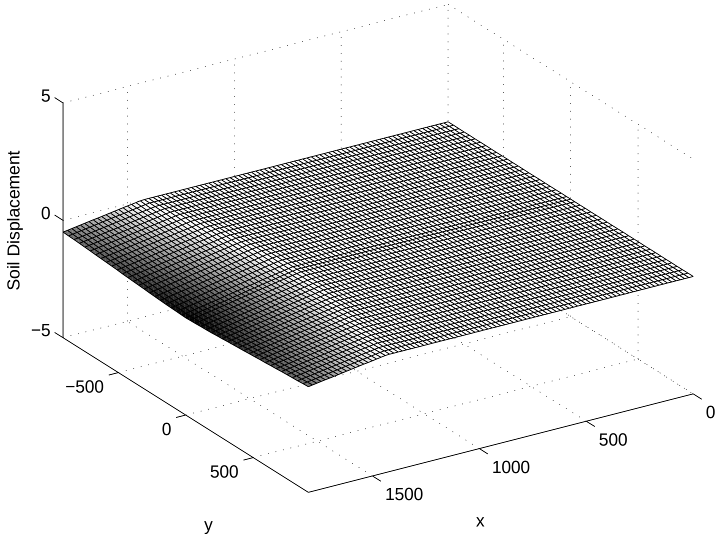

Figure 4.6: Soil displacement, beneath the slab, at peak-load.

4.3 Functionally Graded Beams

Prior to studying the effects of various parameters on functionally graded slabs, a simple study is conducted on functionally graded beams. In particular, the effect of fiber content is studied on a beam with two different layers. There are four scenarios reviewed; which are listed in Table 4.2.

Table 4.2: Functionally graded beam types.

Slab	Top Layer	Bottom Layer
1	RCA	RCA
2	RCA w/ fibers	RCA w/ fibers
3	RCA w/ fibers	RCA
4	RCA	RCA w/ fibers

Slab 1 is considered to be the base case for comparison purposes. In addition to the different layering analyzed, the fiber volume fraction is varied. To do this, the total fracture energy of the

FRC cohesive zone elements, described in Figure 2.3, is varied. Previous studies have shown that the ratio of G_{frc} to G_F is approximately 10:1, but to see the effect of this property a small parametric study is carried out in which the ratio in varied between 5:1 and 20:1.

4.3.1 Computational Study of FG Beams

The first scenario simulated is that of a homogeneous, fiber reinforced, RCA concrete beam. The setup and resulting load-CMOD curves are shown in Figure 4.7. The results show that, as the fracture energy of the fiber reinforced concrete layer increases, a proportional increase in post peak-load carrying capacity occurs. These results can be explained by referencing the effect of increasing G_{frc} on the cohesive zone model illustrated in Figure 3.10. As G_{frc} increases, the initial penalty stiffness and peak-load of the cohesive model remain unchanged, while the softening region increases considerably.

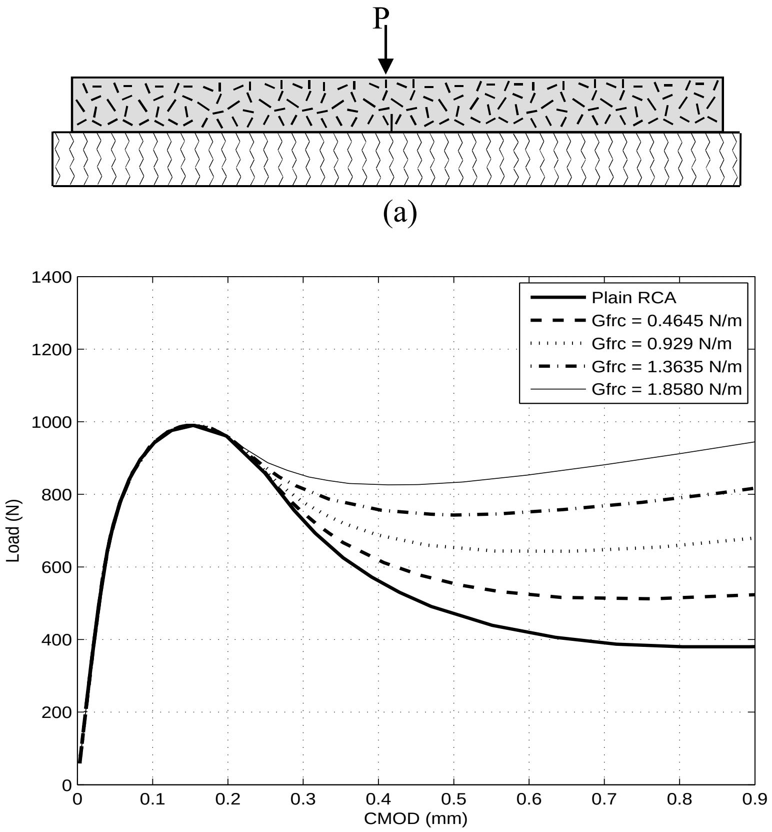

(a)

(b)

Figure 4.7: (a) Beam setup (b) Effect of FRC fracture energy on the behaviour of homogeneous RCA slabs.

In the second scenario considered, the beam is layered and the fibers are confined to the bottom half of the anticipated fracture surface. The load setup and results are illustrated in Figure 4.8. Again, this scenario yields a larger load carrying capacity immediately after the peak-load, increasing with increasing G_{frc}. The load carrying capacity shows a sudden drop off after a while. This likely has to do with the sudden transition between the fiber reinforced layer and the plain layer.

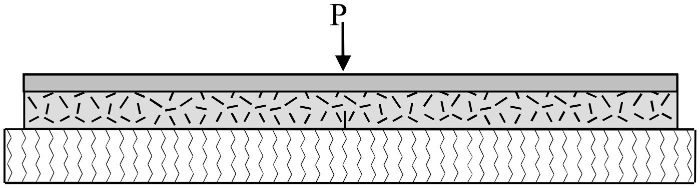

(a)

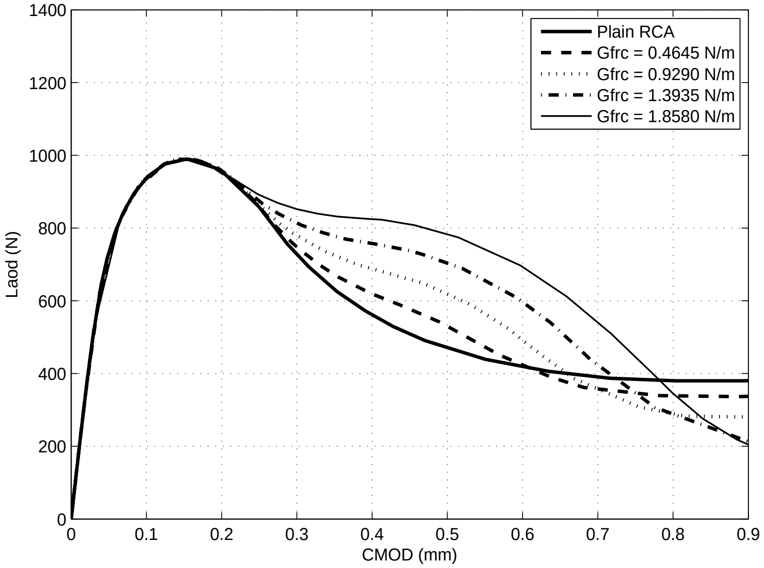

(b)

Figure 4.8: (a) Beam setup (b) Effect of FRC fracture energy on the behaviour of layered RCA slabs with fibers on bottom.

The final scenario to consider is that in which the beam is layered with the fibers confined to the top half of the anticipated fracture surface. The load setup and results are shown in Figure 4.9.

In this case, the results show that the post peak-load behaviour is similar to that of a fully homogeneous, fiber reinforced slab. The load carrying capacity that the beam is able to resist after the peak-load has been reached increases with increasing G_{frc}. Interestingly, when the G_{frc} reaches a value of 1.8580 N/m, it affects the peak-load, increasing its value by 3.7 percent and shifting it by 0.04 mm.

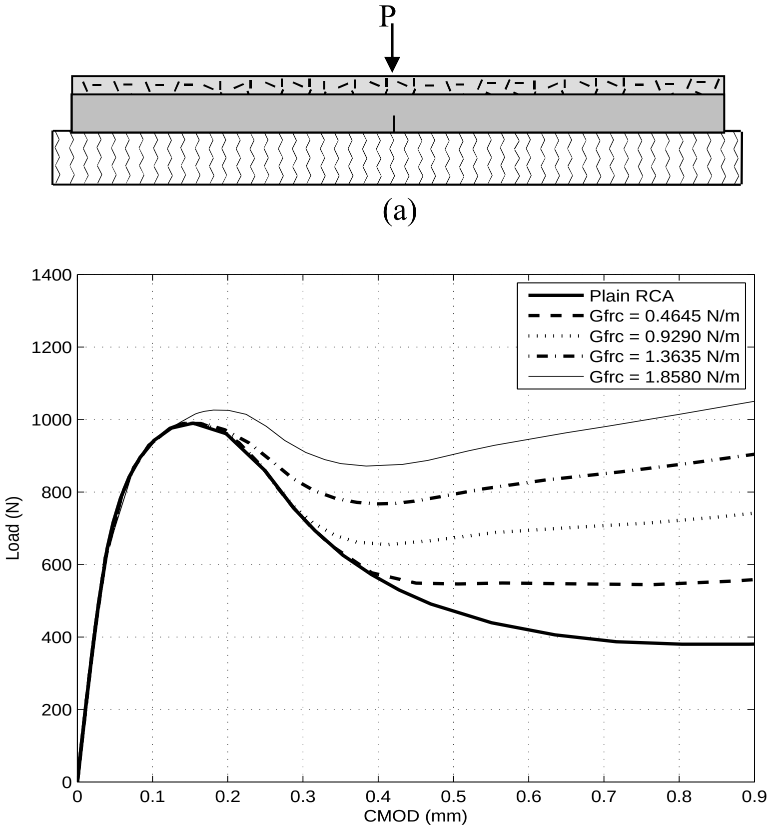

Figure 4.9: (a) Beam setup (b) Effect of FRC fracture energy on the behaviour of layered RCA slabs with fibers on top.

The results of the computational simulations are consistent with experimental observations (Park et al., 2010; Oh et al., 2004; Chunxiang and Patnaikuni, 1999; Gaedicke, 2009).

4.4 Geometric Study of Slabs

In order to optimize and verify the results, an extensive study of the numerical model of the slab is conducted. Two different techniques are chosen for this study. The first technique involves varying the 3D mesh used to represent the slab (an h-refinement). Three different models are created, with different numbers of bulk and cohesive elements. The parameters of each slab are listed in Table 4.3.

The results of the h-refinement study are shown in Figure 4.10. The models show different results, however the differences are not significant. The difference between the peak-loads in the coarse mesh and medium mesh models is about 6kN and between the medium mesh and fine mesh models is about 5kN. Because of the very significant savings in time between the fine mesh model and the medium mesh model, and the relative closeness between the results, the medium mesh model is used throughout the remaining simulations.

Table 4.3: Parameters of slabs used for h-refinement study.

Slab	Number of Bulk Elements	Number of Cohesive Elements	Cohesive Element Size [mm x mm]	Simulation Time [hr]
Fine	1044720	115200	1.25 x 1.25	316
Medium	275220	28800	2.5 x 2.5	40.5
Coarse	190080	14400	1.25 x 10	37.5

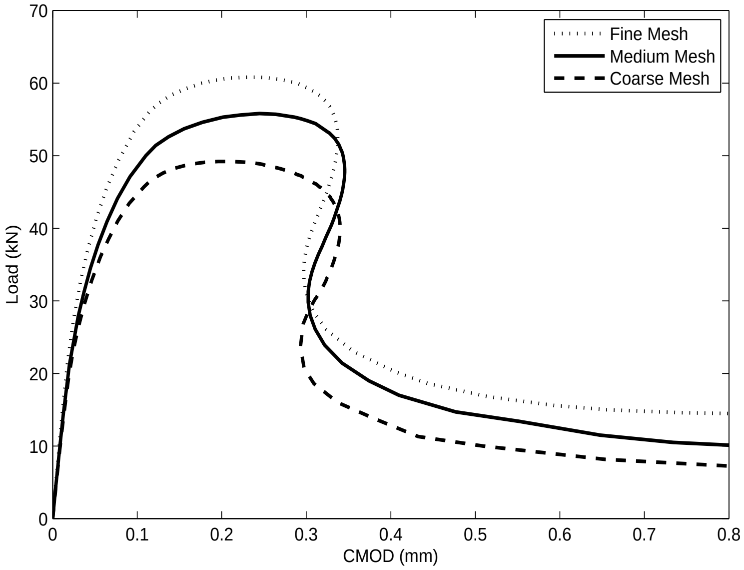

Figure 4.10: Load-CMOD curves resulting from h-refinement study of 3D slab model.

The second technique used to test the model is that of a progressive geometric modification study. The preliminary results show slight snap-back behaviour, so a series of progressive slabs, with varying depth and thickness are simulated in order to help visualize the behaviour. The models and the corresponding results are illustrated in Figures 4.11 and 4.12 respectively.

The results for the progressive depth of slab show an obvious progression. The initial, smallest, depth of 300mm means that the load (located at 150mm from the face of the slab, and 75mm from the crack plane) is at the mid depth of the slab. This loading essentially causes the slab to act as a beam. The load-CMOD curve for this scenario is very much in tune with expected results for a beam test on a soil box. There is a well-defined stiffening and softening portion of the curve, and the load eventually levels off, indicating that the slab has cracked critically and the soil is carrying the majority of the load.

As the slab depth increases there is an obvious trend to the final snap-back results for the full depth (1800mm) slab. The first snap back trend shows up at a depth of about 1200mm, and becomes very apparent by 1500mm.

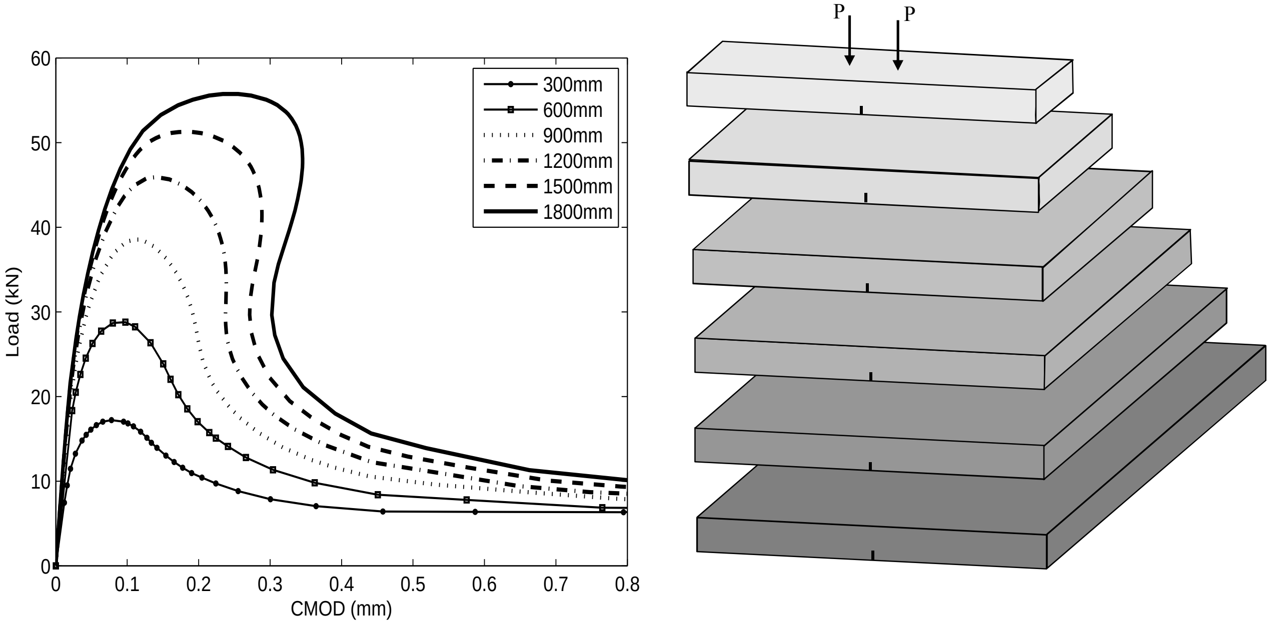

Figure 4.11: Load-CMOD curves for progressive study on slab depth.

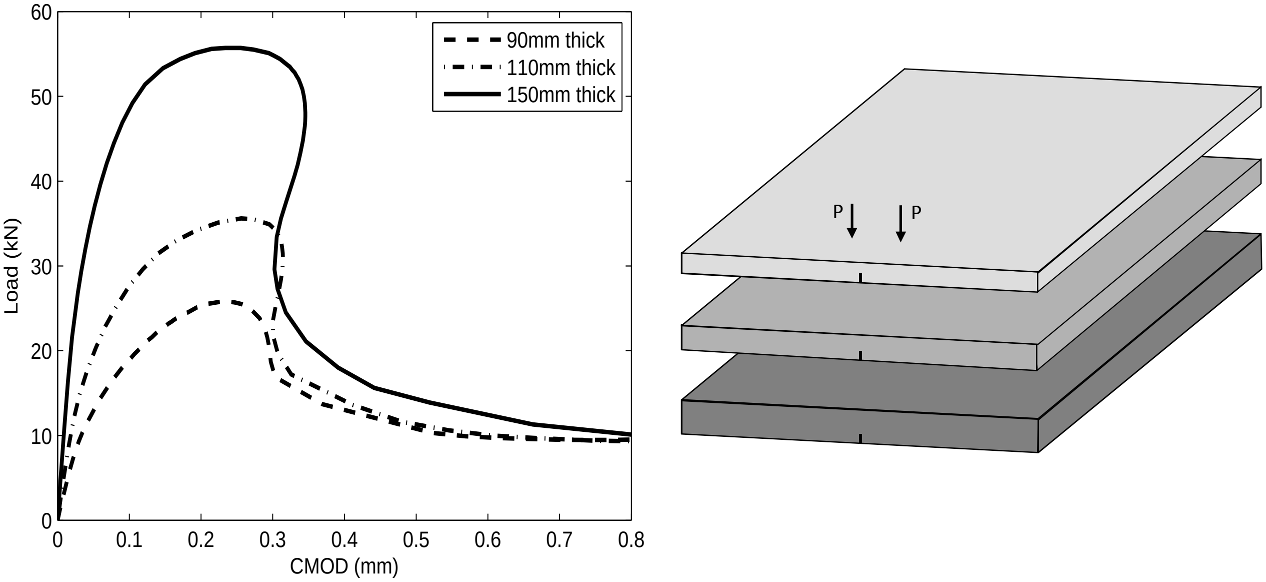

Figure 4.12: Load-CMOD curves for progressive study on slab thickness.

For the case of a progressive thickness of slab (Figure 4.12) three different scenarios are run, 90mm, 110mm, and 150mm thick slabs. The full depth of the slab is used for each simulation, and similar trends are observed in each one. Regardless of the thickness of the slab, snap-back behaviour occurs, indicating that the snap-back behaviour is a by-product of the depth of the slab, not the slab thickness.

The results from the geometric study show that the obtained load-CMOD curves progress naturally from the problem geometry, and that a mesh with 2.5mm x 2.5mm cohesive elements will provide satisfactory results within a reasonable simulation time.

4.5 Direct Comparison of Slabs

Since the experimental results are not available at the time of publication, a direct comparison with each of the slabs is done in order to establish general trends with different configurations. The critical data concerning the peak-loads for the six slabs are listed in Table 4.4. In general, the slabs are all able to carry an average peak-load of 61kN at a CMOD of about 0.27mm. Slabs reinforced with fibers are consistently able to take higher peak-loads at greater CMODs than their plain counterparts. Not surprisingly, the functionally graded slabs display peak-loads and CMODs between those of their homogenous complements.

Table 4.4: Summary of simulation results.

Slab Type	Peak-load (kN)	CMOD at Peak-load (mm)
RCA	56.8	0.249
Lime	60.1	0.302
RCA (fibers)	62.0	0.239
Lime (fibers)	66.0	0.303
Lime/RCA	59.8	0.255
Lime/RCA (fibers)	62.9	0.299

The comparison between the homogenous plain and homogeneous fiber reinforced slabs is shown in Figure 4.13. For both the RCA and LCA cases, adding fibers causes the peak-loads to increase by roughly 10 percent. Also, the softening regions of the curves show much greater post peak-load carrying capacity when fibers are present (about a 65 percent increase). In this study the fibers are assumed to be 40mm long, leading to a final crack opening width of about 13.3mm. Thus, when the slabs develop large macro-cracks, the ones with fiber reinforcing will still be able to carry additional load in the fibers bridging the cracks. This explains the observed increase in the load carrying capacity at large CMOD. Figure 4.14 shows the results comparing the plain homogeneous slabs with the functionally graded slabs. The figure shows that the curve for the functionally graded slab (without fibers) generally falls between the curves for the constituent plain slabs. When fibers are present in the bottom (RCA) layer of the slab, the post peak-load carrying capacity increases by about 55 percent over that in which no fibers are present. This increase in load carrying capacity is less than that of the homogeneously reinforced slabs (Figure 4.13), because only half of the slab is reinforced. The increase is still considerably higher, because the fibers are located close to the initial notch and thus have a larger effect; which is confirmed in previous studies (Roesler et al., 2007a; Park et al., 2010)

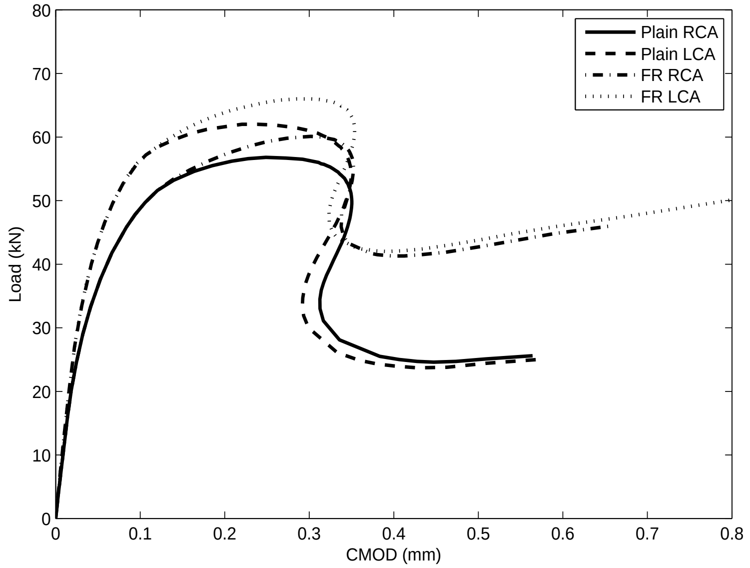

Figure 4.13: Comparison of simulation results for homogeneous slabs.

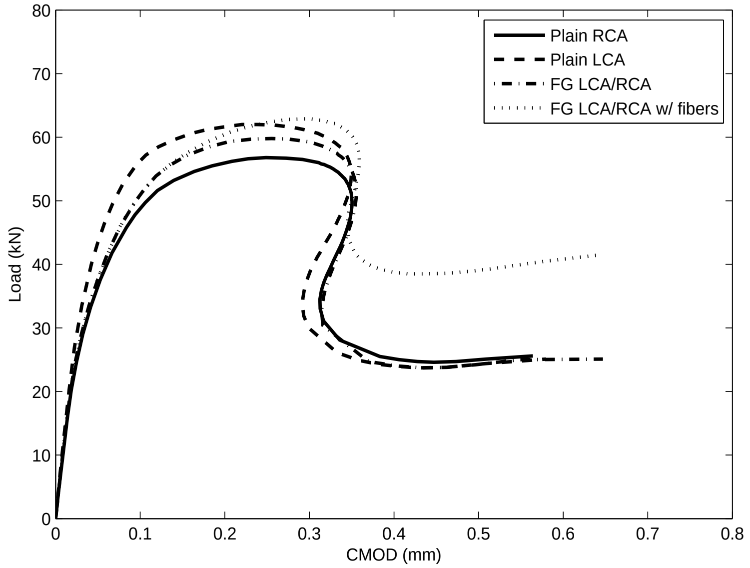

Figure 4.14: Comparison of simulation results between plain slabs and functionally graded slabs.

4.5.1 Slab Cracking Patterns

Figure 4.15 shows two distinct locations along the cohesive zone model that can be defined as the crack front. The leading point of the cohesive zone is the location at which softening initiates. The trailing point of the cohesive zone is the location at which the traction forces vanish and a free surface is created. Using the above two definitions for the crack front, the crack profile of a homogeneous, RCA concrete slab is traced throughout the failure process, see Figure 4.16. In total, ten points along the load-CMOD curve are analyzed.

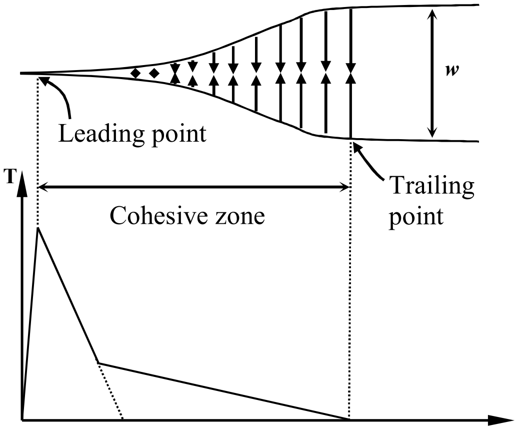

Figure 4.15: Cohesive zone model showing leading point and trailing point.

The profile of the leading point shows a gradual progression to complete failure. Interestingly, the leading point traverses very suddenly through the upper part of the slab, as evidenced by the near vertical portion of the profile in this region. At the peak-load, the crack appears to have gone through half of the slab. Complete cracking, through the depth of the slab, occurs during the snap-back region of the load-CMOD curve.

The profile of the trailing point tends to occur in parallel with, but lag behind, that of the leading point in the lower portion of the slab. The trailing point has a relatively smooth profile throughout the thickness of the slab, without the sudden jump in the upper portion of the slab that is witnessed with the leading point profile. At the peak-load, the crack has extended about one third of the way through the slab. Not shown is the location of complete failure of the slab (when the trailing crack extends all the way through the slab), but this occurs at the initiation of the final stiffening region of the curve. This is the region in which the soil carries the loading from the slab. This has also been observed in preliminary tests done at ATREL, in which the load begins to increase after large macro-cracks appear on the surface of the slab.

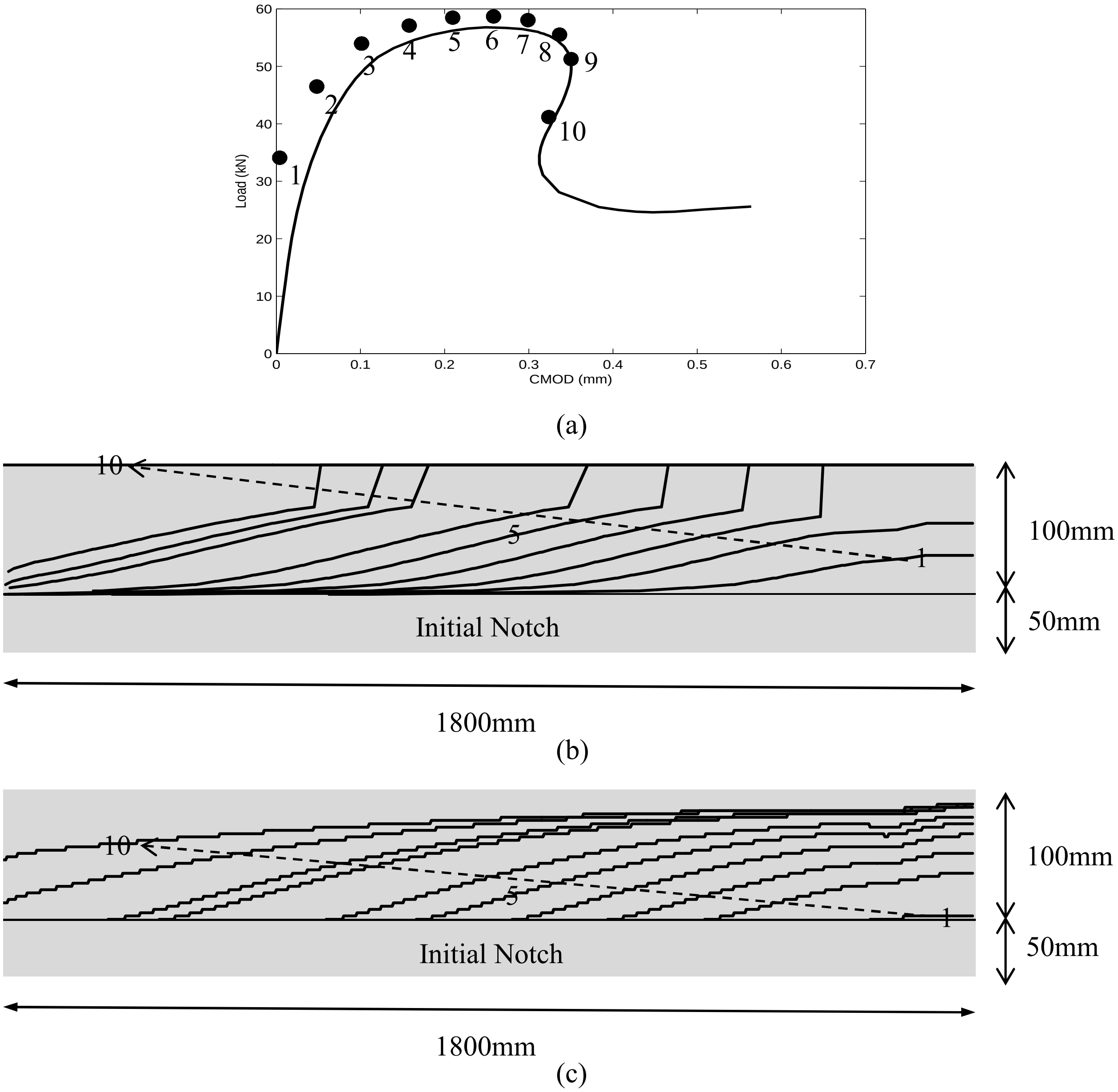

Figure 4.16: (a) Points on load-CMOD curve where the crack front profile is plotted (b) Leading point crack profile (c) Trailing point crack profile (not to scale).

4.6 Parametric Study of Slabs

To determine the effect of the various inputs to the cohesive model on the bulk response of a functionally graded slab, a parametric study is conducted. The study is done on a slab with the top layer consisting of LCA concrete and the bottom layer consisting of fiber reinforced RCA concrete. The parameters of interest include the cohesive strength (f_t), the initial fracture energy (G_f), the total (plain concrete) fracture energy (G_F), and the total (fiber reinforced concrete) fracture energy (G_{frc}). The base case is assumed to be that of the similar slab listed in Table 4.4 and shown in Figure 4.14. The properties of the fiber reinforced RCA concrete layer are the only ones varied in this parametric study, the LCA concrete's properties remain constant. The range of variation for each parameter is listed in Table 4.5. The result of varying each parameter, on the tri-linear traction-separation relationship, is illustrated in Figure 4.17.

Table 4.5: Tri-linear cohesive model input parameter ranges for parametric study.

Specimen	Range	f_t [MPa]	G_f [N/m]	G_F [N/m]	G_{frc} [N/m]
RCA concrete	Min.	1.964	14.04	46.45	464.5
	Base	2.455	17.55	92.90	929.0
	Max.	2.946	21.06	139.35	1393.5

As illustrated in Figure 4.17, the variation of each property has a different effect on the cohesive model. Since the final crack opening displacement w_f is only a function of the fiber length, which is assumed to be a constant, it never changes.

Increasing the cohesive strength (f_t) causes the first kink point in the tri-linear softening region to occur at a lower strength (at the same crack opening displacement). The crack opening displacement at the first kink point is only a function of the critical crack tip opening displacement (CTOD_c), which is assumed to be a constant. The increased cohesive strength also has the effect of shifting the second kink point to occur at a larger crack opening width (at the same strength). The second kink point occurs at essentially the same cohesive strength because the change in each of the parameters that it relies on is minor in comparison to the change in the cohesive strength (Park et al. 2010).

Increasing the initial fracture energy (G_f) causes the first kink point in the tri-linear softening region to occur at a higher strength (at the same crack opening displacement). The second kink point shifts to a smaller crack opening displacement (at the same strength).

Increasing the total fracture energy of plain concrete (G_F) has no effect on the initial portion of the softening model, similar to what was observed in the parametric study done on the bilinear softening curve in Section 3.5. Increasing the total fracture energy of plain concrete causes the second kink point to occur at a larger crack opening displacement and at a lower cohesive strength.

Finally, increasing the total fracture energy of fiber reinforced concrete (G_{frc}) also has no effect on the initial portion of the softening model, but does cause the second kink point to approach the first kink point in a linear manner. This result is similar to that observed in Figure 2.9.

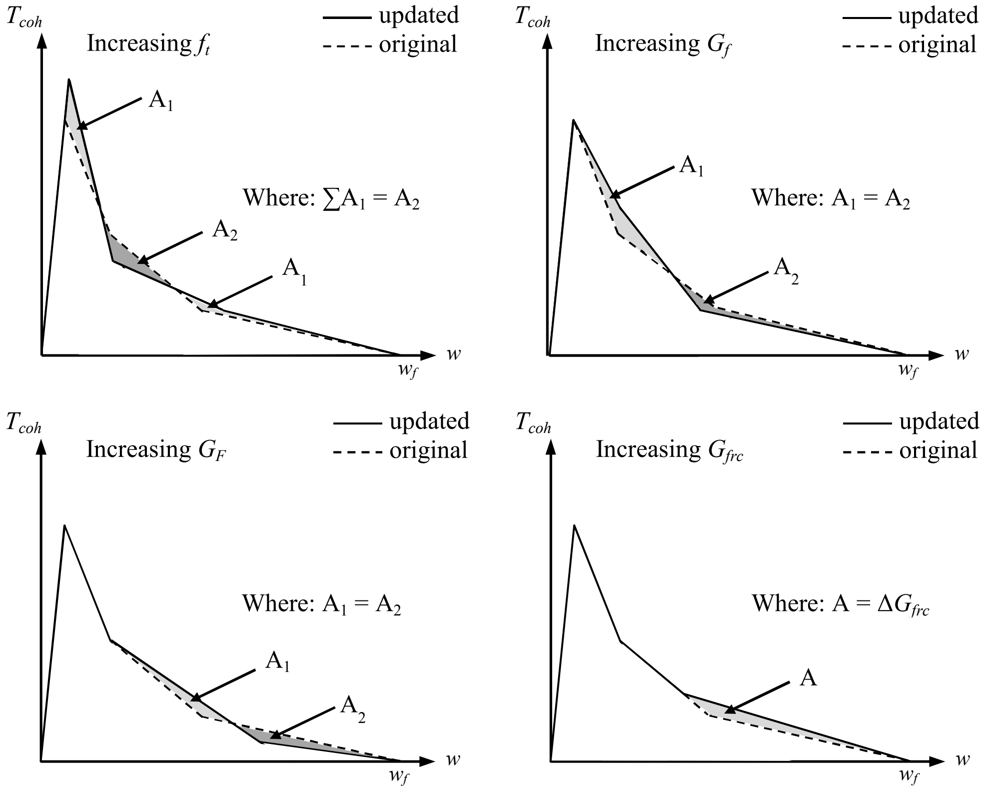

Figure 4.17: Effect of various parameters on the tri-linear cohesive traction separation relationship.

Figure 4.18 shows the effect of varying the cohesive strength on the load-CMOD response of the slab. Very little variation in the response is observed when the cohesive strength is increased or decreased by 20 percent. The peak loads stay the same, and the general trends stay the same regardless of the cohesive strength used in the simulation. This is a positive result, because the cohesive strength is a difficult parameter to quantify. Currently the most common method for choosing the cohesive strength is to use the value of the tensile (or rupture) strength of the concrete. This is purely an estimate, but since the value has very little influence on the response of the slab, this assumption can be considered as acceptable.

When the initial fracture energy is varied by 20 percent the response on the load-CMOD curve is minor but still noticeable, see Figure 4.19. The larger the initial fracture energy, the greater the snap-back feature of the response. When the initial fracture energy decreases by 20 percent; the peak-load decreases by 2.5 percent. This isn't a proportional decrease, since the peak-load increases only 1 percent when the initial fracture energy increases by 20 percent. This result coincides well with the effective change in the cohesive model shown in Figure 4.17. Varying the initial fracture energy has negligible effect on the peak cohesive strength, but has a much greater effect on the behaviour of the softening response. The final, post cracking, stiffening behaviour is identical. This is due to the effect of the soil, as described previously.

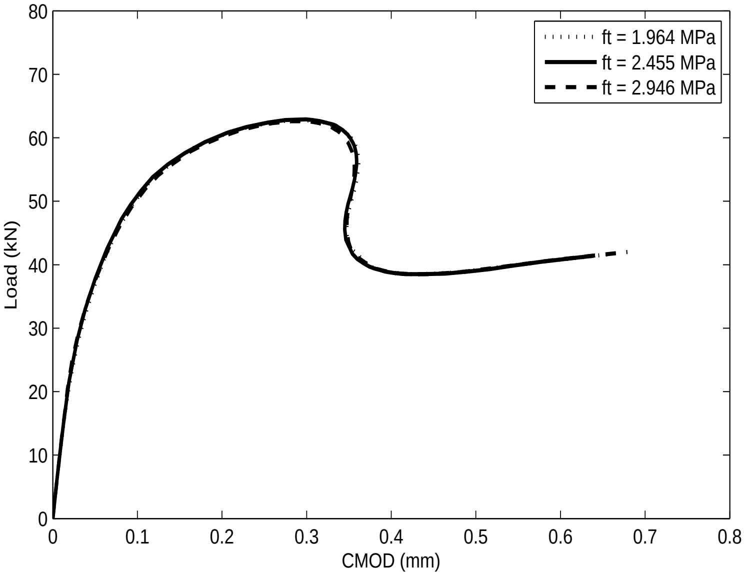

Figure 4.18: Parametric study on the effect of f_t.

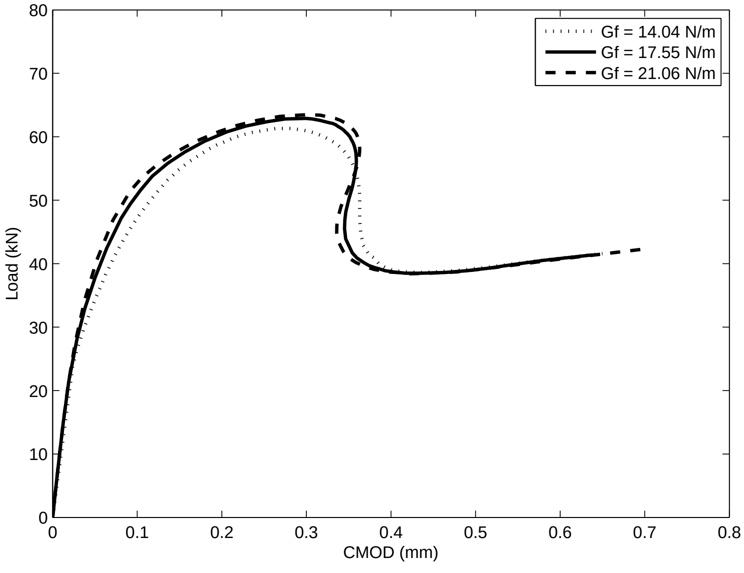

Figure 4.19: Parametric study on the effect of G_f.

The effect of varying the total fracture energy for plain RCA concrete (G_F) is illustrated in Figure 4.20. The effect of increasing G_F by 50 percent causes the peak-load capacity of the slab to increase by 11.5 percent. It does not, however, have a noticeable effect on the CMOD at the peak-load. In each case, the peak-load occurred at a CMOD of 0.3mm. When the G_F decreases by 50 percent; the peak-load capacity of the slab decreases by 14 percent. It also causes the load-CMOD curve to become less gradual in its transition between the hardening and softening regions. The snap-back behaviour remains, but is less pronounced when the G_F is decreased.

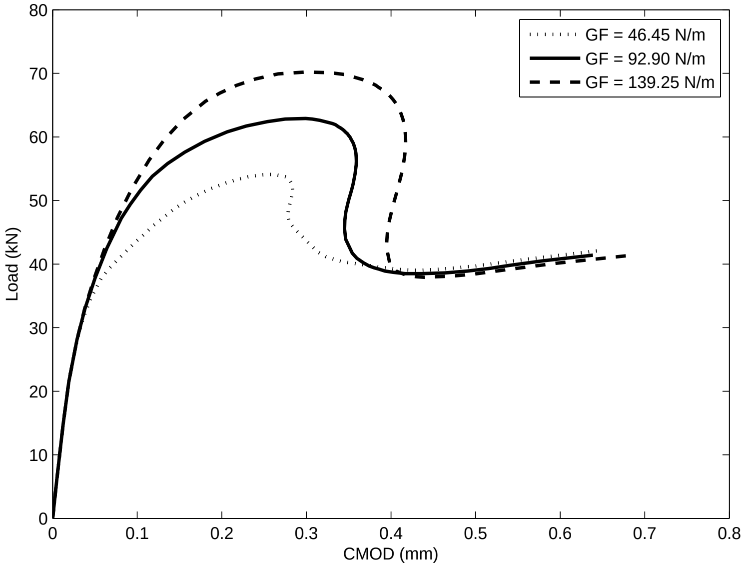

Figure 4.20: Parametric study on the effect of G_F.

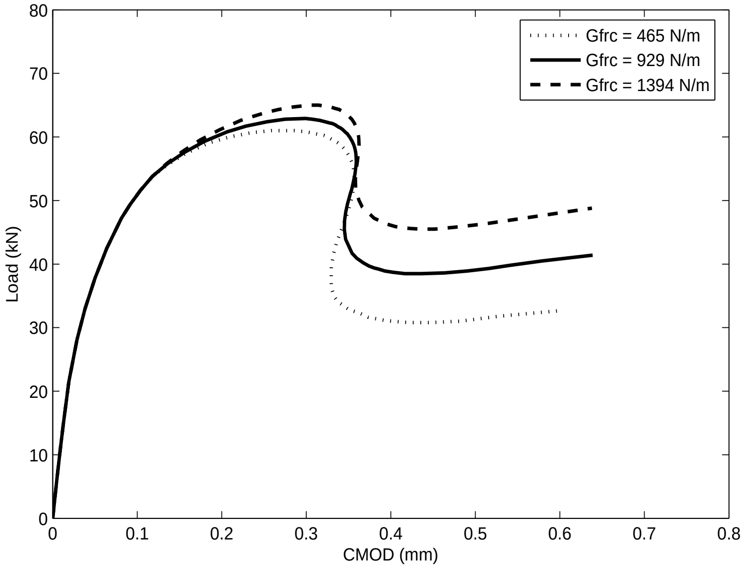

Figure 4.21: Parametric study on the effect of G_{frc}.

The final parameter considered is the total fracture energy of fiber reinforced RCA concrete (G_{frc}). Physically, this can be visualized as varying the fiber volume fraction in the bottom layer of the slab. The effect of increasing the G_{frc} by 50 percent is to increase the peak-load capacity of the slab by 3.3 percent. Also, the softening region of the curve shows a much greater post peak-load carrying capacity (about an 18.5 percent increase). In this study the fibers are assumed to be 40mm long, leading to a final crack opening width of about 13.3mm. Thus, when the slabs develop large macro-cracks, the increased fiber volume fraction will be able to carry additional load in the extra fibers bridging the cracks. This explains the observed increase in the load carrying capacity at large CMOD. Similarly, when the G_{frc} in decreased by 50 percent, the peak-load capacity of the slab decreases 3.0 percent, and the post peak-load carrying capacity decreases by about 20 percent.

CHAPTER 5

CONCLUSIONS AND FUTURE WORK

This study presents a computational framework for modeling the fracture of sustainable concrete materials. A new test specimen is proposed and an in depth look into the failure of functionally graded slabs is conducted. This chapter presents some of the contributions of this work, and provides suggestions for future work.

5.1 Concluding Remarks

This work first provides an overview of the computational methods of implementing cohesive zone elements and functionally graded elements into an existing finite element analysis program. A number of cohesive element formulations are discussed and mathematically outlined. The formulations are then implemented into a commercial finite element program (ABAQUS) using user defined elements (UELs). After that, a new concrete test specimen, designed to allow for easier extraction of fracture properties from existing structures, is proposed. A finite element model of the test specimen is then created and seeded with cohesive elements containing experimentally determined fracture parameters. The experiments and model are then correlated (in a feedback loop), to develop a clear method for predicting the fracture properties of sustainable concrete structures. Examples of the experimental and computational results are compared to confirm the applicability of the specimen and model. A parametric study is conducted to quantify the relative errors in the response, due to the assumed properties.

The already established cohesive element formulations are then extended to three dimensions and utilized to model a functionally graded slab. Due to the absence of experimental data, a purely computational investigation of the response of sustainable, functionally graded slabs is conducted. A series of simulations are run on six different slab configurations. Comparisons are made between the response of the slabs to one another, and conclusions are drawn based on the resulting load-CMOD curves. Finally, a parametric study is conducted on the miscellaneous fracture parameters chosen for the sustainable concrete material, in order to quantify the changes due to assumed quantities.

The primary contributions in this study are briefly summarized as:

- The development of a new test specimen (and its corresponding geometric correction factors) which is able to accurately predict the mode I fracture parameters of existing concrete structures.
- A thorough computational study on the applicability of simple sustainable concrete structures to resist loads. Functionally graded beams as well as functionally graded slabs are simulated, and compared. The results of the beam simulations are in agreement with those determined from previous studies. There have been no experiments conducted on functionally graded slabs to verify the results.

5.2 Suggestions for Future Work

The work in this study makes some assumptions that could not be tested. Additionally, the materials used in this study are restrictive and could be expanded. Below are five suggestions for potential areas of future work. They are listed in the order that they relate to the work done in this study.

5.2.1 Extrapolation of DCT properties

The DCT test specimen is proposed as a simple test used to obtain the fracture properties of concrete structures. However, there are some well-established tests that do just this; such as, the SENB test. It would be beneficial to be able to use the DCT test results to predict the SENB test results, allowing correlation between the new DCT results and the vast banks of SENB data available. This could potentially be extended to predict the load capacity of several simple geometries of concrete, including beams and slabs.

5.2.2 Effect of Aggregate Inclusions

When modelling the bulk concrete material, this study assumes a homogeneous medium with experimentally determined properties. This is the most common method used in the industry, but concrete is actually a very random material with a distribution of aggregates, cement and air pockets. On a large scale such as a slab, the effect of this distribution can often be ignored. The behaviour of the slab is usually governed by the overall contribution of the slab, not an individual aggregate or air pocket. On a small scale; however, such as that for the DCT test specimen, a single aggregate can have a large impact on the fracture surface and corresponding fracture properties. A study could be conducted on the DCT test specimen to quantify the effect of percent aggregate content and percent air content on the resulting load-CMOD response.

5.2.3 Mixed Mode Applications

The current study assumes a simplified, mode I fracture surface; allowing for simplistic modelling and analysis. In reality, the fracture surface displays slight mixed mode tendencies, see Figure 5.1.

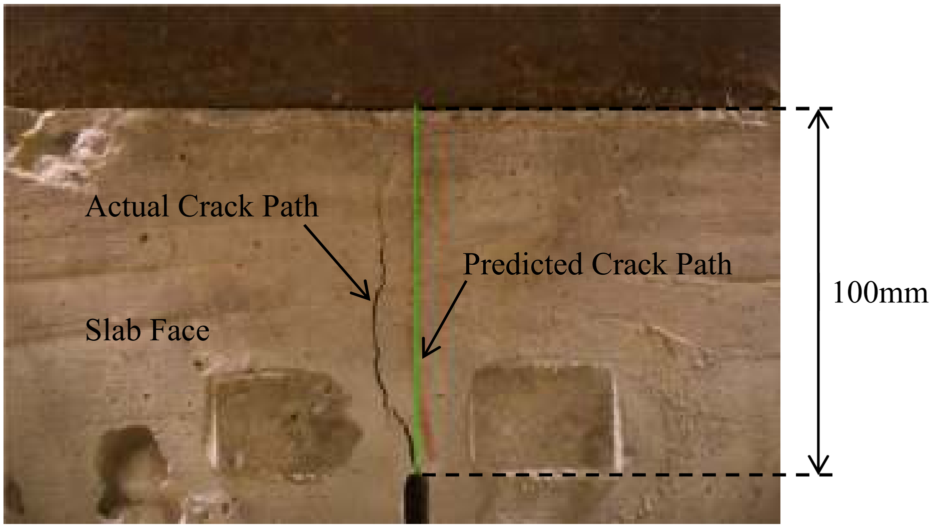

Figure 5.1: Crack path above initial notch.

The study can be extended to a mixed mode analysis of functionally graded materials using extrinsic, potential based, cohesive zone models; such as, the Park-Paulino-Roesler (PPR) model. The PPR model is unique in that it is able to simulate problems with different mode I and mode II fracture energies (Zhang 2007). The extrinsic CZM approach will allow for insertion of cohesive elements where needed and when needed. For a simulation of this size and complexity, adaptive refinement and coarsening would likely be useful to help reduce the computational time.

5.2.4 Soft Materials

This study focuses on the application of various CZM's to model the fracture of different types of concrete. Concrete is a quasi-brittle material and is a very common application for the use of CZM's. Soft materials, such as asphalt, rubber, biological tissue, and many polymers are ductile, and have very different failure mechanisms (Persson, 1999; Wan et al., 2003; Dave, 2009). Modelling these materials can often be difficult, and modelling their fracture is even more difficult. CZM's could potentially be used to help model their failure, by modifying the cohesive models to allow for more gradual stiffening, and a more ductile softening.

5.2.5 Rate Dependent Materials

The fracture, fatigue and delamination of asphalt overlays on highways and airfield pavement infrastructure are a major problem in the United States (Dave et al., 2010). Asphalt is a viscoelastic, functionally graded composite material. To accurately simulate these failure mechanisms in asphalt slabs; the current, functionally graded cohesive zone model could be expanded to a rate-dependent, functionally graded cohesive zone model. An experimental study, with a feedback loop between experiments and simulations could be conducted which would allow for calibration between the model and experimental data.

REFERENCES

ABAQUS. (2002). Version 6.2, Hibbitt, Karlsson and Sorensen Inc., Pawtucket, RI.

ACI Committee 555. (2002). Removal and reuse of hardened concrete. *ACI Materials Journal.* Vol. 99, No. 3, pp. 300-325.

Akçaolu T, Tokyay M., Celik T. (2004). Effect of coarse aggregate size and matrix quality of ITZ and failure behaviour of concrete under uniaxial compression. *Cement and Concrete Composites*. Vol. 26, No. 6, pp. 633-638.

Amirkhanian, A. (2010). Functionally graded concrete pavement system [*PowerPoint slides*] Department of Civil and Environmental Engineering, UIUC, Referenced January 2010.

ASTM D7313-07b. (2007). Standard method for determining fracture energy of asphalt-aggregate mixtures using the disk-shaped compact tension geometry, ASTM International.

Banthia, N. (1997). Fibre reinforced concrete: Present and future. Proceedings from the Asia-Pacific Specialty Conference on Fibre Reinforced Concrete, CI-Premier Singapore, pp. 1–10.

Barenblatt G. I. (1959). The formation of equilibrium cracks during brittle fracture. General ideas and hypotheses. Axially-symmetric cracks. *Journal of Applied Mathematics and Mechanics*. Vol. 23, No. 3, pp. 622-636.

Barros da S. Santos Neto, Almir, La Rovere, Henriette Lebre. (2010). Composite concrete/GFRP slabs for footbridge deck systems. *Composite Structures*. Vol. 92, No. 10, pp. 2554-2564

Barros, J. A. O., Figueiras, J. A. (1998). Experimental behaviour of fibre concrete slabs on soil, *Mechanics of Cohesive Frictional Materials,* Vol. 3, No. 3, pp. 277-290.

Bažant, Z. P. (1991). Fracture mechanics of quasi-brittle structures: Recent advances. *Proc., 11th International Conference on Structural Mechanics in Reactor Technology.* Tokyo, August, ed. By H. Shibita, Vol. H, Paper H04/1, pp. 97-107.

Bažant, Z. P., Qiang, Y., and Goanseup, Z. (2002a). Choice of standard fracture test for concrete and its statistical evaluation. *International Journal of Fracture*. Vol. 118, No. 4, pp. 303-337.

Bažant, Z. P. (2002b). Concrete fracture models: Testing and practice. *Engineering Fracture Mechanics*. Vol. 69, No. 2, pp. 165-205.

Berto, Arnaldo Moreno. (2007) Ceramic tiles: Above and beyond traditional applications. *Journal of the European Ceramic Society*, Vol. 27, No. 2-3, pp. 1607-1613.

Camacho G.T., and Ortiz M. (1996), Computational modeling of impact damage in brittle materials. *International Journal of Solids and Structures* Vol. 33, No. 20-22, pp. 2899-938.

Chunxiang, Q., Patnaikuni, I. (1999) Properties of high-strength steel fiber-reinforced concrete beams in bending. *Cement and Concrete Composites*. Vol. 21, No. 1, pp. 73-81.

.

Dave, E. (2009). Asphalt pavement aging and temperature dependent properties using functionally graded viscoelastic model. PhD Dissertation. Department of Civil and Environmental Engineering, UIUC.

Dave, E. V., Buttlar, W. G., Paulino, G. H. (2010). Asphalt pavement aging and temperature dependent properties through a functionally graded viscoelastic model, Part II: applications. Proceedings of the Multiscale, Multifunctional, and Functionally Graded Materials Conference (FGM2008).

Dugdale D. S. (1960). Yielding of steel sheets containing slits. *Journal of Mechanics and Physics of Solids*. Vol. 8, No. 2, pp. 100-104.

Eischen, J.W. (1987). Fracture of nonhomogeneous materials, *International Journal of Fracture*. Vol. 34, No. 1, pp. 3-22.

El-Ragaby, A., El-Salakawy, E., Benmokrane, B. (2007). Life evaluation of concrete bridge deck slabs reinforced with glass FRP composite bars. *Journal of Composites for Construction*. Vol. 11, No. 3, pp. 258-268.

Giaccio, G., Zerbino, R. (1998). Failure mechanism of concrete: Combined effects of coarse aggregates and strength level. *Advanced Cement Based Materials.* Vol. 7, No. 2, pp. 41-48.

Goldberg, R.K., and Hopkins, D.A. (1995). Thermal analysis of functionally graded material subject to a thermal gradient using the boundary element method, *Composites Engineering.* Vol. 5, No. 7, pp. 793-806.

Guinea, G. V., Planas, J., and Elices, M. (1994). A general bilinear fit for the softening curve of concrete. *Materials and Structures.* Vol. 27, No. 166, pp. 99–105.

Gustafsson, A., and Hillerborg, P. J. (1985). Improvements in concrete design achieved through application of fracture mechanics. *NATO ASI Series, Series E: Applied Sciences*. No. 94, pp. 667-680.

Hansen, T. C. (1986). Recycled aggregate and recycled aggregate concrete, second state-of-the-art report, developments from 1945-1985. *Materials and Structures*. Vol. 19, No. 111, pp. 201-246.

Hansen, T. C. (1992). Recycling of demolished concrete and masonry, *RILEM Report*, No. 6, E&FN Spon, London, Great Britain, pp. 316.

Ilschner B. (1996). Processing-microstructure-property relationships in graded materials. *Journal of the Mechanics and Physics of Solid*. Vol. 44, No. 5, pp. 647-56.

Ilschner, B. (1999). Technical resume of the 5th international symposium on functionally graded materials. *Materials Science Forum Volumes 308-311*, pp. 3-10.

Imamoto, K., Kimura, Y., Nagayama M., Tamura H. (2004). Deflections and cracking of full scale specimens with recycled coarse aggregate concrete processed by a decompression and rapid release. *Journal of the Society of Materials Science*. Vol. 53, No. 10, pp. 1071-1076.

Katz A. (2003). Properties of concrete made with recycled aggregate from partially hydrated old concrete. *Cement and Concrete Research*. Vol. 33, No. 5, pp.703-11.

Kaufmann, J., Lübben, J., Schwitter, E. (2007). Mechanical reinforcement of concrete with bi-component fibers. *Composites Part A: Applied Science and Manufacturing*. Vol. 38, No. 9, pp. 1975-1984.

Khaloo, A. R., Afshari, M. (2004). Flexural behavior of small steel fibre reinforced concrete slabs. *Cement and Concrete Composites*. Vol. 27, No. 1, pp. 141-149.

Kim J. H., Paulino G. H. (2002). Isoparametric graded finite elements for nonhomogeneous isotropic and orthotropic materials. *ASME Journal of Applied Mechanics*, Vol. 69, No. 4, pp. 502-514.

Kou, S. C., Poon, C. S., Chan, D. (2007). Influence of fly ash as cement replacement on the properties of recycled aggregate concrete. *Journal of Materials in Civil Engineering*. Vol. 19, No. 9, pp. 709–718.

Nataraja, M. C., Dhang, N., Gupta, A. P. (2000). Toughness characterization of steel fiber-reinforced concrete by JSCE approach. *Cement and Concrete Research*. Vol. 30, No. 4, pp. 593-597.

Nemat-Alla, M. (2003). Reduction of thermal stresses by developing two-dimensional functionally graded materials. *International Journal of Solids and Structures*, Vol. 40, No. 26, pp. 7339-56.

Newman Jr. J. C. (1979). Stress intensity factors and crack opening displacements for round compact specimens. Report: NASA-TM-80174. 36p.

Newman Jr. J. C. (1981). Stress intensity factors and crack opening displacements for round compact specimens," *International Journal of Fracture*, Vol. 17, pp. 567-578.

Nixon, P. J. (1978). Recycled concrete as an aggregate for concrete – a review., *Materials and Structures*. Vol. 11, No. 65, pp. 371-378.

Oh, B. H., Park, D. G., Kim, J. C., Choi, Y. C. (2004). Experimental and theoretical investigation on the post cracking behavior of synthetic fiber reinforced concrete beams. *Cement and Concrete Research*. Vo. 35, No. 2, pp. 384-392.

Olivito, R. S., Zuccarello, F. A. (2009). An experimental study on the tensile strength of steel fiber reinforced concrete. *Composites Part B: Engineering*. Vol. 41, No. 3, pp. 246-255.

Ortiz M., and Pandolfi A. (1999). Finite-deformation irreversible cohesive elements for three-dimensional crack propagation analysis. *International Journal for Numerical Method in Engineering* Vol. 44, No. 9, pp. 1267-1282.

Otsuki, N., Miyazato, S., Yodsudjai, W. (2003). Influence of recycled aggregate on interfacial transition zone, strength, chloride penetration and carbonation of concrete. *Journal of Materials in Civil Engineering*. Vol. 15, No. 5, pp. 443-451.

Ozturk, M., and Erdogan, F. (1997). Mode I crack problem in an inhomogeneous orthotropic medium. *International Journal of Engineering Science*. Vol. 35, No. 9, pp. 869-883.

Park, K. (2005). Concrete fracture mechanics and size effect using a specialized cohesive zone model. MS Thesis, Department of Civil and Environmental Engineering, UIUC.

Park, K., Paulino, G. H., and Roesler, J. R. (2008). Determination of the kink point in the bilinear softening model for concrete. *Engineering Fracture Mechanics.* Vol. 75, No. 13, pp. 3806-3818.

Park, K., Paulino, G. H., and Roesler, J. R. (2010). Cohesive fracture model for functionally graded fiber reinforced concrete. *Cement and Concrete Research*. Vol. 40, No. 6, pp. 956-965.

Paulino, G. H., Zhang, Z. (2005). Dynamic fracture of functionally graded composites using an intrinsic cohesive zone model. Materials Science Forum. Vols. 492-493, pp. 447-452.

Persson, B. N. J. (1999). Fracture of polymers. *Journal of Chemical Physics*. Vol. 110, No. 19, pp. 9713-9724.

Petersson, P. E. (1981). Crack growth and development of fracture zone in plain concrete and similar materials. Report No. LUTVDG/TVBM-1006/1-174/(1981), 177p.

Pindera, M.-J., and Dunn, P. (1997). Evaluation of the higher-order theory for functionally graded materials via the finite-element method, *Composites Part B: Engineering*. Vol. 28, No. 1-2, pp. 109-119.

Poon, C. S., Shui, Z. H., Lam, L. (2004). Effect of microstructure of ITZ on compressive strength of concrete with recycled aggregates. *Construction and Building Materials*. Vol. 18, No. 6, pp. 461-468.

RILEM, 1994 Recommendation. 121-DRG guidance for demolition and reuse of concrete and masonry. Specifications for concrete with recycled aggregates. *Materials and Structures*. Vol. 27, No. 9, pp. 557-559.

Roesler, J. R., Paulino, G. H., Gaedicke C., Bordelon, A., Park, K. (2007a). Fracture behavior of functionally graded concrete materials for rigid pavements. *Transportation Research Record* No. 2037, pp. 40-49.

Roesler, J. R., Paulino, G. H., Park, K. and Gaedicke, C. (2007b). Concrete fracture prediction using bilinear softening. *Cement and Concrete Composites.* Vol. 29, No. 4, pp. 300–312.

Santare, M. H., and Lambros, J. (2000). Use of graded finite elements to model the behavior of nonhomogeneous materials. *ASME Journal of Applied Mechanics*, Vol. 67, No. 4, pp. 819-822.

Shen, B., Hubler, M., Paulino G. H., Struble, L. J. (2008). Functionally graded fiber-reinforced cement composite: processing, microstructure, and properties. *Cement and Concrete Composites*. Vol. 30, No. 8, pp. 663-673.

Shen, Bin. (2009). Functionally graded fiber-reinforced cementitious composites – manufacturing and extraction of cohesive fracture properties using finite elements and digital image correlation. PhD Dissertation, Department of Civil and Environmental Engineering, UIUC.

Song, S. H. (2006). Fracture of asphalt concrete: A cohesive zone modeling approach considering viscoelastic effects. PhD Thesis, Department of Civil and Environmental Engineering, UIUC.

Song, S. H., Paulino, G. H., Buttlar, W. G. (2006a). A bilinear cohesive zone model tailored for fracture of asphalt concrete considering viscoelastic bulk material. *Engineering Fracture Mechanics*. Vol. 73, No. 18, pp. 2829-2848.

Song, S. H., Paulino, G. H. Buttlar, W. G. (2006b). Simulation of crack propagation in asphalt concrete using an intrinsic cohesive zone model. *ASCE Journal of Engineering Mechanics*. Vol. 132, No. 11, pp. 1215-1223.

Tada, H., Paris, P. C., and Irwin, G. R. (2000). The stress analysis of cracks handbook. New York: ASME Press.

Vancura, M., Khazanovich, L., Tompkins, D. (2009). Reappraisal of recycled concrete aggregate as coarse aggregate in concretes for rigid pavements. *Journal of the Transportation Research Board*, No. 2113, pp. 149-155.

Wan, Y. P., Fang, D. N., Soh, A. K., Hwang, K. C. (2003). Effect of magnetostriction on fracture of a soft ferromagnetic medium with a crack like flaw. *Fatigue and Fracture of Engineering Materials and Structures*. Vol. 26, No. 11, pp. 1091-1102.

Watari F, Yokoyama A, Matsuno H, Saso F, Uo M and Kawaski T. (1999). Biocompatibility of titanium/hydroxyapatite and titanium/cobalt functionally graded implants. *Materials Science Forum*. Vol. 308-311, pp. 356-361.

Wittmann, F. H., Rokugo, K., Brühwiler, E., Mihashi, H., Simopnin, P. (1988). Fracture energy and strain softening of concrete as determined by compact tension specimens. *Materials and Structures*. Vol. 21, No. 121, pp. 21–32.

Wosko, M., Paszkiewicz, B., Piasecki, T., Szyszka, A., Paszkiewicz, R., Tlaczala, M. (2005). Photonics and Microsystems. *Proceedings of 2005 International Students and Young Scientists Workshop*; (IEEE Cat. No.05EX1073), pp. 87-9.

Xu X.P., and Needleman A. (1994). Numerical simulations of fast crack growth in brittle solids. *Journal of the Mechanics and Physics of Solids*. Vol. 42, No. 9, pp. 1397-1434.

Zhang, Z. (2007). Extrinsic cohesive modeling of dynamic fracture and microbranching instability using a topological data structure. PhD Thesis. Department of Civil and Environmental Engineering, UIUC.

Zhou, J., Wang X., Yo T. (2008). Mechanic behavior test on recycled concrete simply-supported rectangular slabs. *Journal of Shenyang Jianzhu University (Natural Science)*, Vol. 24, No. 3, pp. 411-415.

APPENDIX: ABAQUS USER SUBROUTINE FOR A THREE-DIMENSIONAL, FUNCTIONALLY GRADED, TRI-LINEAR COHESIVE ELEMENT

```
c ------------------------------ 3D Functionally Graded Tri-Linear UEL ------------------------------ c
c                                   Written by: Daniel Spring                                        c
c                                 Modified On: November 12th, 2010                                   c
c                              Advisor: Professor Glaucio H. Paulino                                 c
c ---------------------------------------------------------------------------------------------------- c
c
c References:
c
c 1) ABAQUS. (2002). Version 6.2, Hibbitt, Karlsson and Sorensen Inc.,
c Pawtucket, RI.
c
c 2) Song, S. H., (2006). Fracture of Asphalt Concrete: A Cohesive
c Zone Modeling Approach Considering Viscoelastic Effects. PhD
c Thesis, Department of Civil and Environmental Engineering, UIUC.
c
c 3) Park, K. (2005). Concrete fracture mechanics and size effect using
c a specialized cohesive zone model. MS Thesis, Department of Civil
c and Environmental Engineering, UIUC.
c
c 4) Park, K., Paulino, G.H., Roesler, J. (2010). Cohesive fracture model for
c functionally graded fiber reinforced concrete. Cement and Concrete
c Research. Vol. 40, No. 6, pp. 956-965.
c
c 5) Kim J. H., Paulino G. H. (2002). Isoparametric graded finite
c elements for nonhomogeneous isotropic and orthotropic materials.
c ASME Journal of Applied Mechanics, Vol. 69, No. 4, pp. 502-514.
c
=================================================================
      SUBROUTINE UEL (RHS, AMATRX, SVARS, ENERGY, NDOFEL, NRHS, NSVARS,
     & PROPS, NPROPS, COORDS, MCRD, NNODE, U, DU, V, A, JTYPE, TIME,
     & DTIME, KSTEP, KINC, JELEM, PARAMS, NDLOAD, JDLTYP, ADLMAG,
     & PREDEF, NPREDF, LFLAGS, MLVARX, DDLMAG, MDLOAD, PNEWDT, JPROPS,
     & NJPROP, PERIOD)
c
      INCLUDE 'ABA_PARAM.INC'
c
      DIMENSION RHS(MLVARX,*),AMATRX(NDOFEL,NDOFEL),PROPS(*),
     & SVARS(*),ENERGY(8),COORDS(MCRD,NNODE),U(NDOFEL),
     & DU(MLVARX,*),V(NDOFEL),A(NDOFEL),TIME(2),PARAMS(*),
     & JDLTYP(MDLOAD,*),ADLMAG(MDLOAD,*),DDLMAG(MDLOAD,*),
     & PREDEF(2,NPREDF,NNODE),LFLAGS(*),JPROPS(*)
c
      DIMENSION ds1(4),ds2(4),dn(4),Trac(MCRD,NRHS),
```

```
     & Trac_Jacob(MCRD,MCRD),R(MCRD,MCRD),coord_l(MCRD,NNODE),
     & GP_coord(2),sf(4),B(MCRD,NDOFEL),co_de_m(3,4),
     & B_t(NDOFEL,MCRD), Transformation_M(NDOFEL,NDOFEL),
     & Transformation_M_T(NDOFEL,NDOFEL),temp1(MCRD,NDOFEL),
     & stiff_l(NDOFEL,NDOFEL),temp2(NDOFEL,NDOFEL),
     & stiff_g(NDOFEL,NDOFEL),residual_l(NDOFEL,NRHS),
     & residual_g(NDOFEL,NRHS),aJacob_M(2,3),delu_loc_gp(mcrd),
     & co_de(mcrd,nnode)
c ====================================================================
c Variables to be updated in the subroutine
c       RHS = Right hand side vector
c       AMATRX = Stiffness (Jacobian) matrix
c Variables available in the subroutine
c       U = displacement vector
c       COORDS = Original coordinates of the nodes of the element
c       MCRD = Number of coordinates (3 for 3D case)
c       NNODE = Number of number per element
c Inputs to the UEL (PROPS)
c       G_f = Total fracture energy of plain concrete
c       G_f1 = Initial fracture energy of plain concrete
c       f_t = Rupture strength of plain concrete
c       CTOD = Critical crack tip opening displacement
c       fL = Average length of fiber
c       w_ratio = ratio of w_cr to w_f
c       G_min = Minimum fiber reinforced concrete fracture energy (~G_f)
c       G_max = Maximum fiber reinforced concrete fracture energy
c       Zmin = Z coordinate of minimum frc fracture energy
c       Zmax = Z coordinate of maximum frc fracture energy
c Constants used to define traction-separation relationship
c       w_1 = Intercept of crack opening axis and initial descending slope
c       w_f = final crack opening displacement
c       w_k1 = Crack opening displacement at first slope change
c       psi1 = Stress at first change of slope
c       w_2 = Intercept of crack opening axis and secondary descending slope
c       psi2 = Stress at second change of slope
c       w_k2 = Crack opening displacement at second slope change
c       w_cr = critical crack opening width (where peak strength occurs)
```

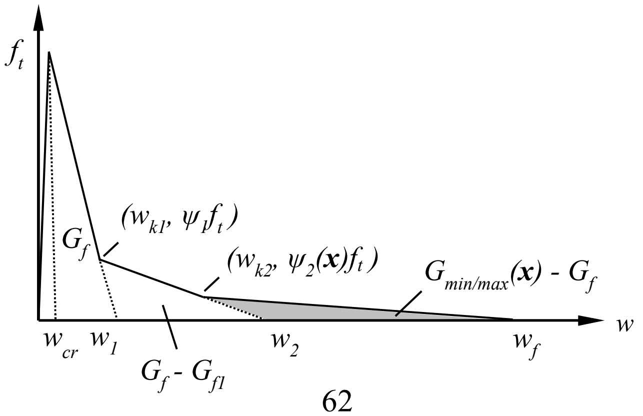

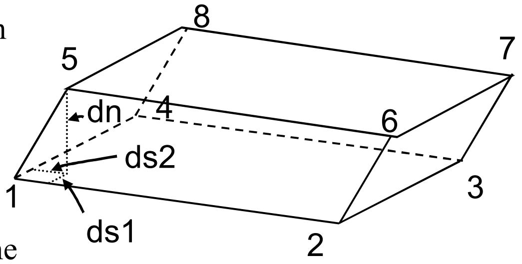

```
c Variables used during calculations
c       ds1 = opening displacement in one shear direction
c       ds2 = opening displacement in second shear direction
c       dn = opening displacement in normal direction
c       Trac = Cohesive force law vector
c       Trac_Jacob = Derivative of the cohesive law matrix
c       R = Coordinate transformation matrix
c       coord_l = local coordinates of brick element
c       GP_coord = coordinates of Gauss points on mid-plane
c       B = Strain-displacement matrix
c       B_t = Transpose of B matrix
c       co_de_m = coordinates of mid-plane of brick element
c       Transformation_M = Local-global transformation matrix
c       Transformation_M_T = Transpose of Transformation_M
c       stiff_l = Stiffness matrix in local coordinates
c       stiff_g = Stiffness matrix in global coordinates
c       residual_l = load vector in local coordinates
c       residual_g = load vector in global coordinates
c       aJacob_M = Jacobian matrix
c       delu_loc_gp = normal and shear opening displacement matrix
c                          (calculated at gauss points)
c       co_de = Current (deformed configuration) coordinates
c
c Initialize Matrices and Vectors==============================================
c
      call k_vector_zero(ds1,4)
      call k_vector_zero(ds2,4)
      call k_vector_zero(dn,4)
      call k_matrix_zero(Trac,mcrd,nrhs)
      call k_matrix_zero(Trac_Jacob,mcrd,mcrd)
      call k_matrix_zero(R,mcrd,mcrd)
      call k_matrix_zero(coord_l,mcrd,nnode)
      call k_vector_zero(GP_coord,2)
      call k_vector_zero(sf,4)
      call k_matrix_zero(Transformation_M,ndofel,ndofel)
      call k_matrix_zero(Transformation_M_T,ndofel,ndofel)
      call k_matrix_zero(B,mcrd,ndofel)
      call k_matrix_zero(B_t,ndofel,mcrd)
      call k_matrix_zero(temp1,mcrd,ndofel)
      call k_matrix_zero(stiff_l,ndofel,ndofel)
      call k_matrix_zero(temp2,ndofel,ndofel)
      call k_matrix_zero(stiff_g,ndofel,ndofel)
      call k_matrix_zero(residual_l,ndofel,nrhs)
      call k_matrix_zero(residual_g,ndofel,nrhs)
      call k_matrix_zero(aJacob_M,2,3)
      call k_matrix_zero(co_de_m,3,4)
```

```
      call k_matrix_zero(rhs,ndofel,nrhs)
      call k_matrix_zero(amatrx,ndofel,ndofel)
      call k_matrix_zero(co_de,mcrd,nnode)
      a_Jacob=0.d0
c
c Update current coordinates (including displacements)==============================
c
      do i = 1, mcrd
        do j = 1, nnode
          co_de(i,j)=coords(i,j)+u(3*(j-1)+i)
       end do
      end do
c
c Do local computations===================================================
c
      call k_local_coordinates(R,coord_l,Transformation_M,
     & Transformation_M_T,a_Jacob,aJacob_M,coords,co_de_m,U,ndofel,
     & nnode,mcrd,co_de)
c
c Compute shear and normal local opening displacements============================
c
      do i = 1, 4
        ds1(i)=coord_l(1,i+4)-coord_l(1,i)
        ds2(i)=coord_l(2,i+4)-coord_l(2,i)
        dn(i) =coord_l(3,i+4)-coord_l(3,i)
      end do
c
c Do Calculations at Gauss Points============================================
c
      do i = 1, 4
c
c Determine the values of the shape function at each Gauss Point
c
        call k_shape_fun(i,sf)
        call k_vector_zero(delu_loc_gp,mcrd)
c
c Determine shear and normal opening displacements at Gauss points
c
        do j = 1, 4
          delu_loc_gp(1)=delu_loc_gp(1)+ds1(j)*sf(j)
          delu_loc_gp(2)=delu_loc_gp(2)+ds2(j)*sf(j)
          delu_loc_gp(3)=delu_loc_gp(3)+ dn(j)*sf(j)
        end do
c
c Define Inputs to UEL
c
```

```
      G_f=props(1)
      G_f1=props(2)
      f_t=props(3)
      CTOD=props(4)
      fL=props(5)
      w_ratio=props(6)
c
c Determine Inputs to Cohesive Model
c
      w_1=(G_f1/f_t)*2.d0
      w_f=fL*(1.d0/3.d0)
      w_k1=CTOD
      psi1=1-CTOD*f_t/(G_f1*2.d0)
      w_2=(2/(psi1*f_t))*(G_f-(1-psi1)*G_f1)
c
c Calculate variation of FRC fracture energy
c Get max and min FRC values
      G_min=props(7)
      G_max=props(8)
      delGfrc=G_max-G_min
c Coordinates of where max and min fracture energy occur
      Zmin=props(9)
      Zmax=props(10)
c Calculate coordinates of mid-plane nodes
      z1=co_de_m(3,1)
      z2=co_de_m(3,2)
      z3=co_de_m(3,3)
      z4=co_de_m(3,4)
c Calculate FRC fracture energy at nodes of mid-plane
      Gfrc1=G_min+((Zmax-z1)/(Zmax-Zmin))*delGfrc
      Gfrc2=G_min+((Zmax-z2)/(Zmax-Zmin))*delGfrc
      Gfrc3=G_min+((Zmax-z3)/(Zmax-Zmin))*delGfrc
      Gfrc4=G_min+((Zmax-z4)/(Zmax-Zmin))*delGfrc
c Get current gauss point and corresponding shape function values
      call k_vector_zero(GP_coord,2)
      call k_Get_Gauss_Points(i,GP_coord)
      ks=GP_coord(1)
      kt=GP_coord(2)
      sf11=0.25*(1-kt)*(1-ks)
      sf22=0.25*(1-kt)*(1+ks)
      sf33=0.25*(1+kt)*(1+ks)
      sf44=0.25*(1+kt)*(1-ks)
c Calculate Fracture energy at current Gauss point
      G_frc=sf11*Gfrc1+sf22*Gfrc2+sf33*Gfrc3+sf44*Gfrc4
c
      psi2=2*(G_frc-G_f)/(f_t*(w_f-w_2))
```

```
      w_k2=w_2-(psi2/psi1)*(w_2-w_k1)
      w_cr=w_ratio*w_1
c
c Determine Traction vector and tangent modulus matrix
c
        call k_cohesive_law(Trac,Trac_Jacob,f_t,psi1,psi2,w_1,
     & w_2,w_k1,w_k2,w_f,w_cr,delu_loc_gp,mcrd,nrhs)
c
c Determine B matrix and its transpose
c
        call k_Bmatrix(sf,B,mcrd,ndofel)
        call k_matrix_transpose(B,B_t,mcrd,ndofel)
c
c Compute the stiffness matrix
c Local Stiffness = B_t * Trac_Jacob * B
c
        call k_matrix_multiply(Trac_Jacob,B,temp1,mcrd,mcrd,
     & ndofel)
        call k_matrix_multiply(B_t,temp1,stiff_l,ndofel,
     & mcrd,ndofel)
c
c Compute Global stiffness matrix
c Global_K = T' * K * T
c
        call k_matrix_multiply(Transformation_M_T,stiff_l,
     & temp2,ndofel,ndofel,ndofel)
        call k_matrix_multiply(temp2,Transformation_M,stiff_g,
     & ndofel,ndofel,ndofel)
c
c Multiply Jacobian with the Global stiffness and add contribution
c from each Gauss Point
c
        call k_matrix_plus_scalar(amatrx,stiff_g,a_Jacob,
     & ndofel,ndofel)
c
c Compute the global residual vector
c Local_residual = B_t * Trac
c Global_residual = T' * Local_residual
c
        call k_matrix_multiply(B_t,Trac,residual_l,ndofel,
     & mcrd,nrhs)
        call k_matrix_multiply(Transformation_M_T,residual_l,
     & residual_g,ndofel,ndofel,nrhs)
c
c Multiply the Global residual by the Jacobian and add the
c contribution from each point
```

```
c
       call k_matrix_plus_scalar(rhs,residual_g,a_Jacob,
     & ndofel,nrhs)
      end do
c
      return
      end
c =====================================================================
c ==========================SUBROUTINES==========================
c =====================================================================
c
c Determine the strain-displacement (B) matrix
c
      subroutine k_Bmatrix(sf,B,mcrd,ndofel)
      INCLUDE 'ABA_PARAM.INC'
      dimension sf(4),B(mcrd,ndofel)
      B(1,1) =  sf(1)
      B(1,4) =  sf(2)
      B(1,7) =  sf(3)
      B(1,10)=  sf(4)
      B(1,13)= -sf(1)
      B(1,16)= -sf(2)
      B(1,19)= -sf(3)
      B(1,22)= -sf(4)
      B(2,2) =  sf(1)
      B(2,5) =  sf(2)
      B(2,8) =  sf(3)
      B(2,11)=  sf(4)
      B(2,14)= -sf(1)
      B(2,17)= -sf(2)
      B(2,20)= -sf(3)
      B(2,23)= -sf(4)
      B(3,3) =  sf(1)
      B(3,6) =  sf(2)
      B(3,9) =  sf(3)
      B(3,12)=  sf(4)
      B(3,15)= -sf(1)
      B(3,18)= -sf(2)
      B(3,21)= -sf(3)
      B(3,24)= -sf(4)
c
      return
      end
c =====================================================================
      subroutine k_cohesive_law(Trac,Trac_Jacob,f_t,psi1,psi2,w_1,
     & w_2,w_k1,w_k2,w_f,w_cr,delu_loc_gp,mcrd,nrhs)
```

```
      INCLUDE 'ABA_PARAM.INC'
      dimension Trac(mcrd,nrhs),Trac_Jacob(mcrd,mcrd),
     & delu_loc_gp(mcrd)
c
c Determine the resulting traction and Jacobian matrix entries
c for shear opening displacements
c
      Trac(1,1)=(f_t/w_cr)*delu_loc_gp(1)
      Trac(2,1)=(f_t/w_cr)*delu_loc_gp(2)
      Trac_Jacob(1,1)=f_t/w_cr
      Trac_Jacob(2,2)=f_t/w_cr
c
c Determine the corresponding traction of an opening displacement
c along the bi-linear cohesive law
c
      if (delu_loc_gp(3) .LE. w_cr) then
        Trac(3,1)=(f_t/w_cr)*delu_loc_gp(3)
        Trac_Jacob(3,3)=f_t/w_cr
      elseif ((delu_loc_gp(3) .GT. w_cr) .and.
     & (delu_loc_gp(3) .LE. w_k1)) then
        Trac(3,1)=(w_1-delu_loc_gp(3))*f_t/(w_1-w_cr)
        Trac_Jacob(3,3)=-f_t/(w_1-w_cr)
      elseif ((delu_loc_gp(3) .GT. w_k1) .and.
     & (delu_loc_gp(3) .LE. w_k2)) then
        Trac(3,1)=(w_2-delu_loc_gp(3))*f_t*psi1/(w_2-w_k1)
        Trac_Jacob(3,3)=-f_t*psi1/(w_2-w_k1)
      elseif ((delu_loc_gp(3) .GT. w_k2) .and.
     & (delu_loc_gp(3) .LE. w_f)) then
        Trac(3,1)=(w_f-delu_loc_gp(3))*f_t*psi2/(w_f-w_k2)
        Trac_Jacob(3,3)=-f_t*psi2/(w_f-w_k2)
      elseif (delu_loc_gp(3) .GT. w_f) then
        call k_matrix_zero(Trac,mcrd,nrhs)
        call k_matrix_zero(Trac_Jacob,mcrd,mcrd)
      end if
c
      return
      end
c ==================================================================
      subroutine k_local_coordinates(R,coord_l,Transformation_M,
     & Transformation_M_T,a_Jacob,aJacob_M,coords,co_de_m,u,ndofel,
     & nnode,mcrd,co_de)
      INCLUDE 'ABA_PARAM.INC'
      dimension R(mcrd,mcrd),coord_l(mcrd,nnode),aJacob_M(2,3),
     & Transformation_M(ndofel,ndofel),coords(mcrd,nnode),
     & Transformation_M_T(ndofel,ndofel),u(ndofel),
     & co_de(mcrd,nnode), co_de_m(3,4),SFD(2,4),GP_coord(2)
```

```
c
c Determine the coordinates of the mid-plane of the brick element
c
      do i = 1, 3
        co_de_m(i,1)=(co_de(i,1)+co_de(i,5))*0.5
        co_de_m(i,2)=(co_de(i,2)+co_de(i,6))*0.5
        co_de_m(i,3)=(co_de(i,3)+co_de(i,7))*0.5
        co_de_m(i,4)=(co_de(i,4)+co_de(i,8))*0.5
      end do
c
c Determine the x, y, and z coordinates of each corner of the mid-plane
c
      x1=co_de_m(1,1)
      x2=co_de_m(1,2)
      x3=co_de_m(1,3)
      x4=co_de_m(1,4)
c
      y1=co_de_m(2,1)
      y2=co_de_m(2,2)
      y3=co_de_m(2,3)
      y4=co_de_m(2,4)
c
      z1=co_de_m(3,1)
      z2=co_de_m(3,2)
      z3=co_de_m(3,3)
      z4=co_de_m(3,4)
c
c Determine the components of two vectors:
c vector "a" along the edge 1-2 of the quadrilateral mid-plane
c vector "b" along the edge 1-4 of the quadrilateral mid-plane
c
      ax=x2-x1
      ay=y2-y1
      az=z2-z1
c
      bx=x4-x1
      by=y4-y1
      bz=z4-z1
c
c Calculate the area (or Jacobian) of the mid-plane using the cross-product
c of vectors "a" and "b"
c
      dum1=ay*bz-az*by
      dum2=az*bx-ax*bz
      dum3=ax*by-ay*bx
c
```

```
      a_Jacob=sqrt(dum1**2+dum2**2+dum3**2)
c ======================================================================
c
c Determine the components of the Jacobian matrix
c
      aJacob_M(1,1)=ax
      aJacob_M(1,2)=ay
      aJacob_M(1,3)=az
      aJacob_M(2,1)=bx
      aJacob_M(2,2)=by
      aJacob_M(2,3)=bz
c
c Determine the components of the rotational matrix R
c
      aLen=sqrt(aJacob_M(1,1)**2+aJacob_M(1,2)**2+aJacob_M(1,3)**2)
      R(1,1)=aJacob_M(1,1)/aLen
      R(1,2)=aJacob_M(1,2)/aLen
      R(1,3)=aJacob_M(1,3)/aLen
c
      aLen1=sqrt(aJacob_M(2,1)**2+aJacob_M(2,2)**2+aJacob_M(2,3)**2)
      R(2,1)=aJacob_M(2,1)/aLen1
      R(2,2)=aJacob_M(2,2)/aLen1
      R(2,3)=aJacob_M(2,3)/aLen1
c
      R(3,1)=R(1,2)*R(2,3)-R(1,3)*R(2,2)
      R(3,2)=R(1,3)*R(2,1)-R(1,1)*R(2,3)
      R(3,3)=R(1,1)*R(2,2)-R(1,2)*R(2,1)
c
      num=nnode
c
c Determine the Transformation Matrix and its transpose
c
      do i = 1, num
        dum=3*(i-1)
        Transformation_M(dum+1,dum+1)=R(1,1)
        Transformation_M(dum+1,dum+2)=R(1,2)
        Transformation_M(dum+1,dum+3)=R(1,3)
        Transformation_M(dum+2,dum+1)=R(2,1)
        Transformation_M(dum+2,dum+2)=R(2,2)
        Transformation_M(dum+2,dum+3)=R(2,3)
        Transformation_M(dum+3,dum+1)=R(3,1)
        Transformation_M(dum+3,dum+2)=R(3,2)
        Transformation_M(dum+3,dum+3)=R(3,3)
      end do
c
      call k_matrix_transpose(Transformation_M,Transformation_M_T,
```

```
     $ ndofel,ndofel)
c
c Calculate the local coordinates of the brick element
c
      do i = 1, nnode
        coord_l(1,i)=(R(1,1)*co_de(1,i)+R(1,2)*co_de(2,i)
     & +R(1,3)*co_de(3,i))
        coord_l(2,i)=(R(2,1)*co_de(1,i)+R(2,2)*co_de(2,i)
     & +R(2,3)*co_de(3,i))
        coord_l(3,i)=(R(3,1)*co_de(1,i)+R(3,2)*co_de(2,i)
     & +R(3,3)*co_de(3,i))
      end do
c
      return
      end
c =====================================================================
      subroutine k_shape_fun(i,sf)
      INCLUDE 'ABA_PARAM.INC'
      dimension sf(4), GP_coord(2)
c
      call k_vector_zero(GP_coord,2)
      call k_Get_Gauss_Points(i,GP_coord)
c
      sf(1)=(1-GP_coord(1))*(1-GP_coord(2))*0.25
      sf(2)=(1+GP_coord(1))*(1-GP_coord(2))*0.25
      sf(3)=(1+GP_coord(1))*(1+GP_coord(2))*0.25
      sf(4)=(1-GP_coord(1))*(1+GP_coord(2))*0.25
c
      return
      end
c =====================================================================
      subroutine k_Get_Gauss_Points(i,GP_coord)
      INCLUDE 'ABA_PARAM.INC'
      dimension GP_coord(2)
c
      if (i .eq. 1) then
        GP_coord(1)=-sqrt(1.0d0/3.0d0)
        GP_coord(2)=-sqrt(1.0d0/3.0d0)
      elseif (i .eq. 2) then
        GP_coord(1)= sqrt(1.0d0/3.0d0)
        GP_coord(2)=-sqrt(1.0d0/3.0d0)
      elseif (i .eq. 3) then
        GP_coord(1)= sqrt(1.0d0/3.0d0)
        GP_coord(2)= sqrt(1.0d0/3.0d0)
      elseif (i .eq. 4) then
        GP_coord(1)=-sqrt(1.0d0/3.0d0)
```

```
         GP_coord(2)= sqrt(1.0d0/3.0d0)
      end if
c
      return
      end
c =====================================================================
      subroutine k_matrix_multiply(A,B,C,l,n,m)
      INCLUDE 'ABA_PARAM.INC'
      dimension A(l,n),B(n,m),C(l,m)
c
      call k_matrix_zero(C,l,m)
c
      do i = 1, l
        do j = 1, m
          do k = 1, n
            C(i,j)=C(i,j)+A(i,k)*B(k,j)
          end do
        end do
      end do
c
      return
      end
c =====================================================================
      subroutine k_matrix_plus_scalar(A,B,c,n,m)
      INCLUDE 'ABA_PARAM.INC'
      dimension A(n,m),B(n,m)
c
      do i = 1, n
        do j = 1, m
          A(i,j)=A(i,j)+c*B(i,j)
        end do
      end do
c
      return
      end
c =====================================================================
      subroutine k_matrix_transpose(A,B,n,m)
      INCLUDE 'ABA_PARAM.INC'
      dimension A(n,m),B(m,n)
c
      do i = 1, n
        do j = 1, m
          B(j,i)=A(i,j)
        end do
      end do
c
```

```
      return
      end
c ============================================================
      subroutine k_matrix_zero(A,n,m)
      INCLUDE 'ABA_PARAM.INC'
      dimension A(n,m)
c
      do i = 1, n
        do j = 1, m
          A(i,j)=0.d0
        end do
      end do
c
      return
      end
c ============================================================
      subroutine k_vector_zero(A,n)
      INCLUDE 'ABA_PARAM.INC'
      dimension A(n)
c
      do i = 1, n
        A(i)=0.d0
      end do
c
      return
      end
c ============================================================
c ===========================END==============================
c ============================================================
```

AUTHOR’S BIOGRAPHY

Daniel William Spring graduated with distinction and co-op standing from the University of British Columbia in 2009 with a Bachelor of Applied Science degree in Civil Engineering. He relocated to Champaign, Illinois, to pursue a graduate degree at the University of Illinois at Urbana-Champaign in August of 2009. Following the completion of his Master’s degree, Daniel will pursue a Ph.D. at the same university.